A generalized mechanical-photonic energy conversion mechanism for photon-generation in piezo-phototronic materials: A case study on commercial piezoelectric alkaline niobates

Bolong Huang[1]*, Mingzi Sun[1], and Dengfeng Peng*[2]

1. *Department of Applied Biology and Chemical Technology, The Hong Kong Polytechnic University, Hung Hom, Kowloon, Hong Kong SAR, China.*

2. *Key Laboratory of Optoelectronic Devices and Systems of Ministry of Education and Guangdong Province, College of Optoelectronic Engineering, Shenzhen University, Shenzhen 518060, China.*

*Email: bhuang@polyu.edu.hk (BH); pengdengfeng@szu.edu.cn (PDF)

Abstract
The creations of photons in response to mechanical stimulus in a crystal that has noncentral symmetry are the great fundamental physics responsible for numbers of important technologies. The underlying mechanism and complete theory for a precise explanation of the mechanical-photonic energy conversion phenomena is vital important. We take commercial piezoelectric $LiNbO_3$ matrics as the example to interpret the detail mechanisms of energy conversions for the photon-generation through a native point defects study. It was found the Frenkel and Schottky type complex pairs as well as the antisite pair defects acting as energy harvesting and migration centers, which are very easy to form and active. It does to be the extra deep electron or hole traps levels near the valence or conduction band edge, respectively. That is the substantial energy reduction via a spontaneous equilibrium transformation from the complementarily charged individuals into agglomerated complexes. Such energy gain for both two processes turns to be independent to the variations of synthesis chemical potentials. In addition, the complex defects actually form independent to the variations of the chemical potentials. This leads to a coupling and exchange effect by them to continuously collect and transport host charges along the path via localized states to the deep recombination levels. The initiating energy barrier is small which ambient thermal stimulation or quantum tunneling can accomplish. The native sensitizers such as V_{Nb2O5}, V_{LiNbO3}, Nb_{Li} are also the energy conversion centers to non-radiative resonant energy transfer onto the activator center at the O_i to transfer the energy into photon emissions. A generalized energy conversion mechanism has been unraveled in this work. This gives a solid theoretical reference for developing the mechanical-photonic energy conversion materials.

Introduction

Mechanically induced photon emission (MIPE) has now been a significant optical phenomenon that aroused considerable interests in material and device applications. Such significant physical picture of energy conversion mechanism illustrates the MIPE materials can be characterized as multi-channel excitation-based photo-energy conversion carriers. They can accept a wide range of wavelength scaled energy excitations, starting from the external UV (ultraviolet) light photo- excitation to near-infra-red (NIR) photo-stimulation or even the extra-long wavelength acoustic or ultrasonic remote stimulations. In addition, they are also highly feasible to accommodate a wide variety of external mechanical stimulation manners, such as pressure, stress, tribo-friction, or ultrasonic waves, which can be efficiently converted into the energies for output photon emissions (luminescence) [1-10]. These external mechanical stimuli have been standardized as measureable and characterizable physical parameters. The resulting electromagnetic light occurs in way of photoemissions. Meanwhile, an observable duration for the emission output decay within the luminescence process indicates the promising application of the persistent phosphorescence.

Based on the plotted energy conversion physical picture (Figure 1), the MIPE provides a novel way of accurately diagnosing the structural health even raw-eye observable, which is far more advantageous over the conventional point-by-point measurement method by use of a strain gage. The multi-scale and multi-dimensional MIPE material will provide a flexible platform of application in fields of earth-quake prediction, stability test of large infrastructures via non-destructive measurement, wearable hand-input oriented multi-touch technology in smartphone or other mobile devices combining with electronics magneto-optelectronics, and even to the promising long-persistent photoacoustic nanogenerators [11-13]. Better understanding the energy conversion mechanism for the MIPE will help us establishing guidelines and a roadmap for developing and materializing the novel MIPE technology.

Recent studies [5, 9, 14-31] demonstrated milestone works in this field that piezo-oxides, oxy-sulfides, sulfides can be easily applied as high-performance MIPE materials through nano-engineering, either transition metal or rare earth ion doping, and achieved flexible color manipulations [32]. This requires us not just only to understand the electronic structures that given by extrinsic doping, but also a high demanding to plot the photon-electron dynamic transitions based on the subtle energy conversion mechanisms towards promising mechano-persistent-luminescence.

As we know, the donor and acceptor charge carriers in the conventional semiconductor materials are usually generated and staying near the conduction (CB) and valence band (VB) edges respectively. Their ionization energy barriers are usually small enough to easily release the free charge carriers to recombination for electronic transitions from high to lower levels. The excited charge carriers will be released back for further spontaneous recombination through the delocalized conduction states of host lattice by a small magnitude of thermal stimulations or quantum tunneling effect. However, most of the piezo-type or non-piezo-type MIPE materials possess the charge carrier levels as extra deep donor and acceptor levels staying near the VB and CB conversely, which brings extra energy consumptions for charge ionization. This also requires a charge alternation process within an equivalent free energy process that alternate the charge localization levels where the donor like level stay at or near the conduction band minimum (CBM) and the acceptor like levels stay at or near the valence band maximum (VBM). The recombination will be a spontaneous process to release the energy in forms of photon emissions. Therefore, the generalized energy conversion and

transfer mechanism study requires us for a descent understanding on the charge carriers alternation process and electronic transition behaviors in the MIPE materials.

The MIPE host materials can be either semiconducting materials (e.g. CaZnOS, $NaNbO_3$ ZnS, nano-ZnO etc.) or insulating materials. Piezoelectric material is one of the important candidates for the MIPE applications [9, 11, 18-31]. Recently, the commercial piezoelectrics LiNbO3, a prominent insulating piezoelectric material, has been reported to be used for high performance red-emitting elastic MIPE with rather high electromechano-optical energy conversions [15]. It shows a superb wide range of photon transparent from 280 nm (ultraviolet) to 5000 nm (far-infrared or micrometer-wave). Its ability for multifunctional control in optoelectronics can be promisingly applied in the field of high- precision sensing of micro-stress, zero-threshold damage diagnosis, or high-resolution bioimaging. Some other MIPE host materials (ZnS, CaZnOS) can be also used for biomedical applications with its biosolvability in the living tissue, single cell, or bone microstructure, e.g. osteoporosis symptom diagnosis with combinations of advanced infra-red (IR)-photoacoustic imaging (tomography).

Herein, the physical picture needs to be more clear that whether the phenomenon of MIPE is limited to the phase of host materials (inorganic or organic) or not. This means a questions arises that what is the essential role of the piezoelectricity? It might not the core reason for originating the MIPE. However, the piezoelectricity is still the essential driving force to produce the local piezoelectric-field within the lattice, in order to form the local ionization potential to facilitate the charge ionization at local defect or impurities sites and promote the inter-site valence exchange type charge transfers. Therefore, there must be a widely valid and generalized energy conversion mechanism to determine and characterize the MIPE beyond the conventional host system.

Calculation method

(1) Thermodynamic limits on chemical potentials of components

Although there have been many experiments reported the synthesis of $LiNbO_3$ mechano-luminescence (ML) materials, it is very difficult to produce the defect-free host because of the stability and purity control, especially for prevention of phase separation. This arises because the host will experience a series of reversible reaction to partial decomposition through the reactions as follows:

$$\mathrm{Li + Nb + (5/2)\ O2 \rightleftharpoons LiNbO3 \rightleftharpoons Li2O + Nb2O5} \quad (1)$$

The formula in Eq. (1) shows a difference and competence of formation enthalpy and chemical potentials of elements and compounds. As pointed out by Xue et al[33], a reaction in the 1 : 1 mixture of Li_2CO_3 and Nb_2O_5 powders (raw precursor materials) may yield not only $LiNbO_3$ but also Li_3NbO_4 and $LiNb_3O_8$ components in the whole system. Following the approach of Ding et al[34], we expand the chemical potentials for Li, Nb, and O as μ_{Li}, μ_{Nb}, and μ_O, respectively. To prevent solid/gas precipitation of these elements in the host lattice, they need to be: $\mu_{Li} \leq 0$, $\mu_{Nb} \leq 0$, and $\mu_O \leq 0$. In realistic equilibrium growth process, the chemical potentials of each constituent species may vary but they are constrained by formation enthalpy of host lattice in order to maintain a stable $LiNbO_3$ compound required as follow:

$$\mu_{Li} + \mu_{Nb} + 3\mu_O = \mu_{LiNbO3} = -14.32\ eV \quad (2)$$

The μ_{LiNbO3} is actually also bound, to avoid the $LiNbO_3$ going through reversible or partial decompositions into Li_2O and Nb_2O_5. They are also bound by thermodynamic relationship formula as follows:

$$\begin{cases} 2\mu_{Li} + \mu_O < \mu_{Li2O} = -6.71\,eV \\ 2\mu_{Nb} + 5\mu_O < \mu_{Nb2O5} = -19.89\,eV \end{cases} \quad (3)$$

The Eq. (2) and (3) also means the differences in their standard formation enthalpy may lead to different stabilities under a high temperature synthesis atmosphere. The aforementioned limitations of chemical potentials are thus be utilized to discuss the stable area for $LiNbO_3$ with respect to the constituent chemical potentials of μ_{Li}, μ_{Nb}, and μ_O, respectively, as constraints (shown in Figure 2). Figure 2 (a)-(c) shows the stable area for different combinations of constituent chemical potentials limits. Figure 2 (c) actually shows a very limited stable area in two-dimensional view with respect to μ_{Li}, μ_{Nb}, and μ_O as constraints, in agreement with the experimental synthesis of $LiNbO_3$ discussed by Marsh et al and Xue et al[33, 35]. Because the Li element is relatively active compared with Nb and O, we thus to list the limits of constituent chemical potentials in way of O-rich and Nb-rich respectively and shown in Table S1.

(2) Ground state structure optimization

The ferroelectric phase of $LiNbO_3$ within *R3c* space group has been chosen for modeling, which is mirror-symmetrical to the lattice of corundum Al_2O_3 (*R-3c*). Since the first Jacob ladder in DFT has been confirmed for reliable structural relaxation and cell optimization of d or even f-orbital based solids [36-38], we use both PBE and PBE+U level CASTEP code [39] for ground state lattice relaxation. The geometry optimization is both well satisfied for both ultrasoft and norm-conserving pseudopotentials. To improve the accuracy of the electronic structure calculation, the Hubbard U parameter has been induced in PBE+U calculations, since it is the key dominant feature that usually underestimated in many semicore d orbital based transition metal oxides.

We chose the (4*s*, 4*p*, 4*d*, 5*s*) states as valence states of Nb, (1*s*, 2*s, 2p*) for Li, and (2s, 2p) for O respectively. We used OPIUM code in the Kleinman-Bylander form norm-conserving pseudopotential [40] with non-linear partial core correction[41] to minimize the systematic error due to the atomic core-valence electron densities overlap. Further the RRKJ method is chosen to optimize the basis sets and ionic minimization of pseudopotentials[42]. The norm-conserving pseudopotentials is chosen because it can reproduce the all-electron behavior for outter shell valence electrons with |**S-matrix**|=1 compared to ultrasoft pseudopotentials[43, 44]. As all of the consituent elements (Li, Nb, and O) are light elements, the spin-orbit coupling effect has not implemented over the calculations. The kinetic cutoff energy of 750eV, which expands the valence electrons states in a plane-wave basis set.

The Nb-related native point defects usually induce the charge-spin out-sync sloshing effect. To guarantee the electronic minimization and convergence, the ensemble DFT (EDFT) method of Marzari et al[45] is used for solving Kohn-Sham equation. The reciprocal space integration was performed by *k*-point sampling with grids of 6 × 6 × 2 *k* points in the Brillouin zone of $LiNbO_3$ unit cell, and 3 × 3 × 2 for defect electronic structures calculations in supercell respectively. We further select the (¼, ¼, 0) special k-point[46] in the size of 2 × 2 × 1 supercell (120-atom sized). This converges the total energy to under $5.0x10^{-7}$eV per atom. The Hellmann-Feynman force on each atom was converged to lower than 0.01eV/Å.

The geometry optimization used the Broyden-Fletcher-Goldfarb-Shannon (BFGS) algorithm through all bulk and defect supercell calculations.

(3) Hubbard-U ab initio determination at each Nb and O site

Because the electronic states in the optical fundamental gap are less sensitive to the nonlinearity of Hubbard U parameters. we choose Anisimov-type rotational-invariant DFT+U method [47]. To minimize the effect of the localized hole states produced by 2p orbitals of O sites, the self-consistently determined Hubbard U potentials is also applied on the O-2p orbitals, which have been reached a consensus [48-51] in many oxides materials. Thus, it is necessary to consider both self-energy corrections on semicore orbitals for oxides [52-54]. However, the non-self-consistently determined Hubbard U parameters usually induce an extra error in lattices due to the non-zero residue of second-order partial derivative to the charge density. It is necessary to consider our established self-consistent determination of U parameter on the electronic structures [37, 51-55], in order to minimize the error on the lattice.

We previously devised a method to ab-initially determine the semicore d/f orbital energy in order to further self-consistently correct the electronic structures from routine first-principles calculations[37, 54, 56]. Our work shows that the method is particularly valid for those materials synthesized via the extremely physical or chemical conditions[37, 54, 56]. The Hubbard U parameter has been self-consistently determined based on our previous developed method[37, 54, 56]. For the all of the electronic states calculations in $LiNbO_3$ models, we use the self-consistent determination for the U correction on the localized Nb-4d orbitals to correct the on-site Coulomb energy of the electron spurious self-energy. With our self-consistently determination process[37, 38, 52-54, 57, 58], the on-site Hubbard U parameters for the partially filled 4d orbitals of Nb is self-consistently determined to be U_d=6.08 eV, and U_p=5.95 eV for O-2p. The detail process was referred to the previous work.

(4) Defect formation enthalpy formula

To calculate defect formation energy calculations at different charge states (q), we consider the overall supercell was established and remained constantly based on the ground state relaxed primitive cell, to avoid the thermodynamic effect of enthalpy changes by cell variations. The formation energy of a targeted defect (H_q) at the specific charge state q, can be described as a relation of the positions of Fermi energy (E_F) and the chemical potential $\Delta\mu$ of species of defects α, which is shown as follow:

$$H_q(E_F,\mu)=\left[E_q-E_H\right]+q\left(E_V+\Delta E_F\right)+\sum_{\alpha} n_\alpha\left(\mu_\alpha^0+\Delta\mu_\alpha\right), \quad (4)$$

The above E_q and E_H are the total energy of a relaxed defective lattice in charge state q and an ideal host lattice at the ground-state, respectively. The ΔE_F in Eq. (4) is the change of Fermi energy with respect to the valence band maximum (VBM, E_V=0), and n_α is the number of atoms of constituent element α chosen as targeted defect sites, then the μ_α^0 is referenced chemical potential, based on the method used by the work of Zunger et al [59].

(5) Charge point defect corrections within the periodic lattice

We consider the case of defects with $q\neq0$ that the Coulomb potential correction is necessary to be used to counteract Madelung the image charge of the crystal lattice. There have been three corrections developed. One is the band alignment correction developed by Van de Walle and coworkers [60]. The second is the dispersion correction of defects between the gamma point and Monkhorst-Pack point, developed by Wei et al. [61]. The third is the

dipole correction, which considers the Madelung effect based on static electric Coulomb potential corrections, developed by Makov and Payne [62]. This method is the current widely used correction scheme in DFT and also implemented in our work. However, such corrections contribute only around ~0.2 eV in magnitude to the defect formation energy. Our goal is to establish a physicochemical trend, rather than highly accurate level calibrations, which require demanding computations.

Results and discussion

Bulk $LiNbO_3$

There have been two stable phases found for the $LiNbO_3$ by experiments, which are ferroelectric (piezoelectric, *R3c*) and paraelectric phases (*R-3c*)[63]. The ground state structure for $LiNbO_3$ at room temperature is the piezoelectric phase (*R3c*). The high-symmetric paraelectric phase (*R-3c*) is stable above 1480 K and can be only stable within a narrow equilibrium region[63]. Thus, the low symmetry structural configuration creates opportunities for the elastic mechano-luminescence (ML) related energy conversions. The crystal lattice of $LiNbO_3$ with space group of *R-3c* has been studied by many groups. It actually follows the ABO_3 perovskite and arranges in a rhombohedral lattice representation studied around by Darlington et al[64]. It has been reported that the local displacement of the Nb-sites and Nb-O octahedron tilting induce the local transition of lattice from (*R3c*)-(*R-3c*)-(*R3m*) symmetry[64]. It indirectly implies that the instabilities of host lattice could be predominantly sourced from the native point defects or defect complexes.

For the structural optimization, the reported crystal lattice parameters of synthesized $LiNbO_3$ are a=5.289 Å and c=13.848 Å determined by Boysen et al through neutron powder scattering experiments[65]. The relaxed structure at the ground state by our linear response DFT+U calculation shows the lattice parameters of a=5.169 Å and c=13.850 Å with very small relative error of 2.27% and 0.01% respectively.

In electronics, the band gap of the $LiNbO_3$ are reported variously from the range of 3.28 (indirect)-4.30 eV (direct) measured by optical absorption experiments. The most frequently used experimental measured band gap is 3.78 eV in ferroelectric phase may have been influenced by the electron-hole attraction induced band gap narrowing effect, and mostly focus on the optical absorption onset position [66-68]. Our calculated band gap (4.13 eV) is much smaller than the 5.28 eV by hybrid-functional calculations and 5.42 eV by GW method, but evidently follows a same magnitude to the 4.71 eV by GW with FLAPW [69-72]. The synthesis of the $LiNbO_3$ usually produce energetically favorable stoichiometric defect such as Li or Nb related vacancy, interstitial or even complex. This may affect the results when the samples are measured in the way of absorption in the vacuum ultraviolet domain or indirect interband transitions [73, 74]. Therefore, the descent understanding on the $LiNbO_3$ requires us to implement a comprehensive and extensive study on the native defects.

From the Figure 3, the ground state electronic band structure calculations based on the optimized cell gives a direct band gap of 4.130 eV following the paths of F→Γ→Z in rhombohedral representation. This results is close to the data of 4.0 eV measured by Redfield et al via temperature varied optical absorption spectroscopy[67]. The calculated optical fundamental band gap is smaller than the 4.30 eV measured by optical absorption of Kase et al[68]. Our calculated band gap data (4.130 eV) is much larger than 3.78 eV from frequently cited experiments[66]. This is due to the exciton-pair induced band gap narrowing effect

during experiment consistent with the analysis by Schimdt et al[75]. Therefore, our DFT+U calculation with ab-inito determined Hubbard-U parameters for fully-occupied Nb $4d^4$ as well as the 2p orbitals for O sites are self-consistent and reliable, which have been also illustrated in our previous work [37, 38, 52-54, 56-58, 76].

Figure 3 also shows the projected components of the (*s*, *p*, *d*) orbital $LiNbO_3$ in TDOS. We see that the top of valence band consists of levels from O-2p orbitals. The lower conduction band is contributed by the Nb-4d orbitals. The O-2s filled orbitals show 12 eV staying below the top of valence band (valance band maximum, VBM).

For the energetics, the bulk properties of crystal $LiNbO_3$, we have already shown the calculated formation enthalpy of piezoelectric $LiNbO_3$ is $\Delta H_f(LiNbO_3)$=-14.32 eV in the Experimental Section with considerations of Eq. (2) and (3). This calculated formation enthalpy shows slightly higher (+0.1 eV, +0.7%) than the one representatively obtained by GGA functional based DFT calculation from Phillpot et al, as well as the experimental data (-14.149 eV) [77]. The formation enthalpies of the sub-components calculations shows that our calculated $\Delta H_f(Nb_2O_5)$=-19.89 eV in a close agreement with experimental measurement of -19.94 eV (+0.2%), and with 1.68 eV higher than the data by Phillpot et al (-18.26 eV) [77]. Our calculated $\Delta H_f(Li_2O)$=-6.71 eV are close to both calculation and experiments [77].

Niobium antisite (Nb_{Li})

We start from the native niobium antisite (Nb_{Li}) defect, which is a possible defect source in energy migration within this ternary compound. This could be seen as the wrongly filling of the interstitial Nb and Li at the intrinsic Nb and Li vacancy sites respectively within $LiNbO_3$. Since only one valence electron for Li, there are four charge states to be discussed for the antisite (Nb_{Li}).

Figure 4 (a) shows the TDOS of the electronic and hole levels that localized within the optical band gap of $LiNbO_3$. The neutral state (Nb_{Li}^0) shows a deep donor trap behavior with the level of 2.84 eV above the VBM (E_V+2.84 eV). The electronic level is actually degenerated with two electronic states staying at the same level. For the Nb_{Li}^+, the defect state shows even deeper donor trap level with position of E_V+2.49 eV. The doubly and triply charged states (Nb_{Li}^{2+} and Nb_{Li}^{3+}) have almost the same electronic and hole levels within the band gap, which are staying at E_V+2.50 eV for the electronic state and E_V+3.97 eV for the hole state, respectively. For the Nb_{Li}^{4+}, the donor trap level turns to be even deeper nearly staying at the midgap, which is E_V+2.13 eV. The localized hole state is staying at the bottom of the CBM with the position of E_V+4.02 eV. For the charge states of +2, +3, and +4, they are all in the spin-down configuration.

As shown in Figure 4 (b), the localized electronic and hole orbitals contour plot have been mapping in the real space lattice of $LiNbO_3$ with consideration of niobium antisite defect (Nb_{Li}). The neutral state shows the two degenerated electronic states occupying the same level is represented by the d_{xy} and d_{yz} components of Nb-4d orbitals staying at Nb_{Li} antisite in spin-up configuration. For the singly and doubly positive charged states (Nb_{Li}^+ and Nb_{Li}^{2+}), the electronic orbitals are nearly the same which are contributed by the d_{xy} component of the Nb_{Li}-4d orbital. However, the localized hole state induced by the Nb_{Li}^{2+} is localized at the second nearest neighboring O and Nb sites from the anti-Li-site (exchanged with Nb), which is contributed by a hybridized orbital between p-π (O) and 4d orbital (Nb) in the lattice. This arises because the local electrical field has been disturbed by the anti-Li-site, and the on-site

orbital charge density distribution has re-arranged to the second nearest cation and anion sites. For the Nb_{Li}^{3+}, the localized electronic state is tilted d_{xy} component of Nb-4d orbital staying at Nb_{Li} site, while the hole state showing the orbitals are localized on the Nb_{Li} site and the second nearest Nb_{host} sites with partial *p-d* coupling effect. For the case of Nb_{Li}^{4+}, the localization of the orbitals is similar to the case found in the Nb_{Li}^{3+}, indicating the valence change of the Nb_{Li} does not change much in the defect charge density distribution within the host, especially under the high charge state (e.g. from Nb_{Li}^{3+} to Nb_{Li}^{4+}). Meanwhile, the electronic orbital contour plot in real-space is nearly the same among the state of Nb_{Li}^{+}, Nb_{Li}^{3+} and Nb_{Li}^{4+}.

We further studied the formation energy of this antisite defect under different charge states, as shown in Figure 4 (c). The cost of energy to form the neutral Nb_{Li} in the host $LiNbO_3$ is 5.55 eV, which is insensitive to the chemical potential limit varied (either O- or Nb- rich), since it is only the exchange of two cation sites within the host following original stoichiometric ratio. The formation of Nb_{Li} is usually achieved by the exchange of Nb and Li sites. Thus, the formation energy for each defect is updated to be 2.77 eV per defect site, i.e. their formation energies should be divided by two as occurrence per defect. The thermodynamic transition level for the state (+/0) staying at E_V+3.93 eV denoting a shallow donor state. However, the Nb_{Li}^{+} state is not a long-life sustained defect state within the host. It will further transform into the Nb_{Li}^{3+} and Nb_{Li}^{4+} with the Fermi level (E_F) varied. Then the transition level for the state (3+/+) is staying at E_V+1.93 eV and (4+/3+) is at E_V+1.75 eV respectively. Among the five different charge states of the Nb_{Li}, there is only the defect reaction shows the negative-U_{eff} with value of -0.03 eV, which is $2Nb_{Li}^{2+} \rightarrow Nb_{Li}^{+} + Nb_{Li}^{3+}$. According to the above analysis, the possible charge states within the optical band gap for Nb_{Li} antisite defect is 0, +1, +3, and +4.

Oxygen anion Frenkel pair defect (a-Fr)

As for the type of lattice distortion, we move on to discuss the charge complementary pair defects, which is another typical intrinsic defects. The lattice distortions are usually caused by the fluctuation of the ambient conditions. The O related anion Frenkel pair (a-Fr) dominates the deep electronic trap levels within the optical band gap, which is important within the metal oxides [52, 57, 78]. We firstly consider the O has been perturbed and dissociated from its original host lattice with evolving into the nearest local cage of the $LiNbO_3$ motif structure.

The TDOS shown in Figure 5 (a) shows the electronic and hole levels induced by the a-Fr (i.e. V_O+O_i) in the lattice. For the a-Fr^0, there are three electronic states with two degenerated in spin-up near the mid gap (E_V+2.48 eV) and one in spin-down next to the VBM (E_V+0.48 eV), as well as one hole state localized next to the CBM in spin-down (E_V+3.89 eV). For the a-Fr^+, one of the degenerated electron has been ionized. The electronic levels are staying in the mid-gap as E_V+2.29 eV (spin-up) and E_V+0.47 eV (spin-down) next to the VBM. Two electronic hole states are localized at E_V+4.00 eV next to the CB edge. For the a-Fr^{2+}, there is only one electron left staying at the E_V+0.49 eV next to the VBM while two hole states staying at E_V+4.05 eV. For the a-Fr^-, the electronic levels are localized at E_V+0.44 eV (spin-up), E_V+2.49 eV (spin-up), E_V+2.53 eV (spin-down), and E_V+2.71 eV (spin-down), respectively. The E_F is pinned at E_V+2.81 eV. The localized hole states are staying at E_V+4.01 eV (spin-up) and degenerated next to the CBM. For the a-Fr^{2-}, all of the localized hole states have been passivated by the excess electrons. There are eight electronic states staying in the gap, which are occupying at the levels of E_V+0.47 eV (spin-up, degeneracy=3),

E_V+0.61 eV (spin-down, degeneracy=2), E_V+2.27 eV (spin-up), E_V+2.51 eV (spin-up), and E_V+2.82 eV (spin-up), respectively.

Figure 5 (b) shows the localized orbitals of electronic and hole states for the aforementioned levels. We see that, for the positively charged states (+1 and +2), all of the mid-gap electronic states are contributed by the V_O part of the a-Fr. These deep donor trap levels are actually dominated by the d_{xy}, d_{xz}, d_{yz}, d_{x2-y2} components of Nb-4d orbitals nearby the V_O site. The localized hole states that staying at the CBM is mainly contributed by the anti-bonding states of the O-2p orbitals at the O_i interstitial site. For the negatively charge states, the electronic state next to the VBM is originated by the coupled p-π electronic orbitals between O_i and nearest neighboring O-sites. The localized hole orbitals next to the CBM are mainly contributed by the p-π* anti-bonding state. The excess electron is pushed forward to the mid-gap by repulsive Coulomb potential and occupying the local Nb-4d orbitals next to the V_O site. Especially to the a-Fr^{2-} charge state, the localized hole states within the band gap have been well passivated by the two excessively captured electrons. Therefore there are only the electronic states localized in the gap mainly distributed at the region next to the VBM or near the mid-gap. In the real-space, these two excess electrons individually have two probabilities of on-site orbital occupations, which are the nearest neighboring Nb-4d orbital at the V_O sites and the other is p-orbitals of O_i site. We also see that the orbitals deep in the gap show an anisotropic p-π non-bonding orbital alignment denoting the trace of the instabilities, which is responsible to the energy-transfer by local electrical fields within the host lattice.

For the formation energy, the cost to form the O-related a-Fr pair defect within the local cage of $LiNbO_3$ motif is relatively high in the neutral, which is 8.22 eV per pair or 4.11 eV per defect site. From Figure 5 (c), we see that only two defect reactions among different charge states give negative-U_{eff}, which are 2a-Fr^- → a-Fr^0 + a-Fr^{2-} and 2a-Fr^0 → a-Fr^{2+} + a-Fr^{2-} with values of -2.40 eV and -1.79 eV, respectively. Therefore, it is indicating that the stable charges for the a-Fr within the host are mainly the +1, +2, and -2. The neutral and singly negative charge states are showing relative life-time to be stabilized within the lattice. However, with overall looking at the Figure 5 (c) along the entire the E_F variation range in the gap, there are only +2 and -2 charge states stable within the optical fundamental band gap area.

Lithium cation Frenkel pair defect (Fr_{Li})

The Li may be very easy to escape from its original lattice and transporting within the host, since the energy cost is found to be rather low for the Li-interstitial (Li_i). Therefore, Li cation Frenkel pair defect (Fr_{Li}) can be very common within the host and may play an active role to affect the local electrical field distribution of the host lattice.

From the TDOS calculation (Figure 6 (a)), the neutral state (Fr_{Li}^0) does not affect the electronic states of host obviously, except only the two electronic states close to the VBM (E_V+0.1 eV). We interpret these levels are attributed to the instabilities of O-2p orbitals near the V_{Li} and the Li_i sites. The singly positive state (Fr_{Li}^+) produce the localized hole states next to the CBM (E_V+3.90 eV). This arises because the hybridized empty p-d orbital components near the V_{Li}. The singly negative state (Fr_{Li}^-) within the host produces two different electronic levels localized in the gap. One of the level staying next to the VBM (E_V+0.10 eV) with two degenerated O-2p electrons while the other level staying at E_V+3.08 eV in the gap contributed by the d_{xy} component of the Nb-4d orbital next to the Li_i site.

The localized electronic and hole orbitals are shown in the Figure 6 (b). The neutral Fr_{Li} state only possess localized O-2p orbitals parallel to the (0001) of the $LiNbO_3$ lattice. The Fr_{Li}^{+} gives the localized hole stats at one pair of O and Nb sites nearby the V_{Li}. The Fr_{Li}^{-} state has two different electronic orbital distribution areas within the lattice. One of them is the localized O-2p orbitals around both V_{Li} and Li_i regions, while the other is staying at the nearest neighboring Nb-4d orbitals at the Li_i site, perpendicular to the $LiNbO_3$ (0001).

The formation energy (Figure 6 (c)) shows the Fr_{Li} is rather energetically favorable within the lattice. The energy cost of the neutral state is 1.31 eV per pair, which means only 0.66 eV per defect site. This result shows a good agreement with the 0.93 eV done by another method from Donnerberg and Catlow coworkers[79]. As we know, the V_O can be seen as a very comment intrinsic defect in the oxide materials confirmed by our previous collaborators [80-82]. However, the formation energy of Fr_{Li} shows even lower level than the V_O under the Nb-rich limit (i.e. 0.66 eV<0.76 eV). Moreover, such Frenkel pair defect is chemical potential limit independent, indicating that the Fr_{Li} is one of the generally existing intrinsic defects in the synthesized LiNbO3 under either Nb-rich or O-rich chemical atmospheres. On the other hand, the Fr_{Li} is a positive-U_{eff} center gives the defect reaction is endothermal process: $2Fr_{Li}^{0} \rightarrow Fr_{Li}^{+} + Fr_{Li}^{-}$ with value of +2.08 eV. The thermodynamic transition levels of the (0/+) state is at E_V+1.64 eV and E_V+3.71 eV for the (-/0) state, showing deep donor and acceptor correspondingly.

Niobium cation Frenkel pair defect (Fr_{Nb})

Another cation Frenkel pair defect in $LiNbO_3$ is the Fr_{Nb}. The Nb atom is perturbed by the thermal vibration or external high energy irradiation, and hopping into the nearby local energetic minimum site from original equilibrium lattice site. This formation may take higher energetic cost and would induce obvious localized electronic levels in the band gap.

The TDOS (Figure 7 (a)) shows that the Fr_{Nb} uniformly induce the localized electronic levels within the band gap without any appearance of the localized hole states. For the Fr_{Nb}^{0}, there are three electronic levels localized within the gap, which are E_V+2.51 eV, E_V+2.85 eV, and E_V+2.99 eV. They are actually the deep donor trap levels. The electronic levels at the singly positive state (Fr_{Nb}^{+}) are slightly different with about 0.1 eV deeper from CBM, which are E_V+2.46 eV, E_V+2.74 eV, and E_V+2.87 eV, respectively. The doubly positive state (Fr_{Nb}^{2+}) shows that one of the electronic level has been terminated and the rest levels are localized at E_V+2.38 eV and E_V+2.73 eV with small ferromagnetic (FM) behavior for the spin-alignment. Differently, both of the Fr_{Nb}^{-} and Fr_{Nb}^{2-} as negatively charge states are showing the trapping of the four localized electronic states in the gap. For the Fr_{Nb}^{-}, the levels are E_V+2.41 eV, E_V+2.68 eV, and E_V+3.08 eV, where the E_V+2.68 eV are doubly degenerated for both spin-up and down electrons. For the Fr_{Nb}^{2-}, the electronic levels are turns even slightly deeper as E_V+2.35 eV, E_V+2.55 eV, and E_V+2.93 eV respectively, where the E_V+2.55 eV are the doubly degenerated level for spin-up and down electrons.

The localized electronic orbitals distributions are shown in Figure 7 (b). We see that all of the electronically active regions induced by the Fr_{Nb} (V_{Nb}+Nb_i) are actually the Nb_i within the local cage of $LiNbO_3$ motif. The electronic levels in the gap are the hybridization of the Nb-4d orbitals between this Nb_i and nearby Nb_{host}. These electronic levels consist of the d-components of d_{xz}, d_{z2}, and d_{xz} of the Nb-4d orbitals.

From the aspect of the energy cost, the formation energy of the neutral Fr_{Nb} is shown as 8.13 eV per pair, which is 4.06 eV per defect site, independent to the chemical potential as either Nb-rich or O-rich limit (Figure 7 (c)). This energy cost is about 6.2 times higher than the Fr_{Li} forms in the host, and also follows well with the trend predicted by the semi-empirical method (6.26 eV)[79]. The defect reactions among different charge states shows it has three negative-U_{eff} processes of $2Fr_{Nb}^{+} \rightarrow Fr_{Nb}^{0} + Fr_{Nb}^{2+}$, $2Fr_{Nb}^{-} \rightarrow Fr_{Nb}^{0} + Fr_{Nb}^{2-}$, and $2Fr_{Nb}^{0} \rightarrow Fr_{Nb}^{2+} + Fr_{Nb}^{2-}$ with values of -1.81 eV, -2.91 eV, and -0.32 eV, respectively, while it also possesses a positive-Ueff reaction for the $2Fr_{Nb}^{0} \rightarrow Fr_{Nb}^{+} + Fr_{Nb}^{-}$ with value of 2.20 eV. Therefore, both of the Fr_{Nb}^{2+} and Fr_{Nb}^{2-} states are the main equilibrium charge states in the host lattice.

Nb_2O_5 Schottky defect (V_{Nb2O5})

The Schottky (STK) defects are also the main intrinsic pair defects that affect the electronic and optical properties of $LiNbO_3$. These are formed by nearest neighbored vacancies that following the stoichiometric ratio of the components within the compound, such as the V_{Nb2O5}, V_{Li2O}, and V_{LiNbO3}. We firstly look at the case of V_{Nb2O5} in the host lattice.

The TDOS calculation (Figure 8 (a)) shows the neutral state (V_{Nb2O5}^{0}) produces two degenerated localized electrons next to the VBM (E_V+0.10 eV) and one localized hole states next to the CBM (E_V+4.08 eV), and there is no mid-gap states. The V_{Nb2O5}^{+} produces one more electronic state localized next to the VBM based on the V_{Nb2O5}^{0}, which are E_V+0.040, E_V+0.060, and E_V+0.10 eV, respectively. The localized hole state almost unchanged the position and stays at E_V+4.09 eV. For the V_{Nb2O5}^{2+} state, the electronic and hole states have similar configurations to the neutral state, which have two degenerated electronic levels at E_V+0.10 eV and E_V+4.10 eV for the localized hole level. This analysis indicates the positive charged states of the V_{Nb2O5} does not provide any mid-gap localized states regardless the electronic and hole levels. However, the region of the V_{Nb2O5} in the host is very active to capture the electrons and to be localized within the mid-gap area. For the V_{Nb2O5}^{-} state, there are two electrons are localized within the band gap with positions of E_V+2.47 eV (spin-down) and E_V+2.60 eV (spin-up), while the localized hole state is at E_V+4.15 eV nearly buried into the CB. For the V_{Nb2O5}^{2-} state, the electronic localization levels within the gap are nearly the same but the spin-configurations are different. These two electronic levels are both spin-up at E_V+2.43 eV and E_V+2.63 eV. The localized hole level is staying at E_V+4.11 eV.

The localized orbitals for the electronic and hole levels are shown in Figure 8 (b). We see that the electronic levels localized nearby VBM induced by positive charge states of V_{Nb2O5} are mainly due to the local distortions of O sites. These distortions further result in the misalignment of the O-2p orbitals and deviated from its equilibrium bonding states from the host. The localized holes induced by these positive charge states are predominantly the anti-bonding Nb-4d orbital levels. For the negatively charged states, both of the localized electrons and hole levels are uniformly contributed by the Nb-4d orbitals that nearby the V_{Nb2O5} site or local void.

Formation energy calculation (Figure 8 (c)) shows this type of intrinsic defects is rather energetically favorable, and showing a similar magnitude to the Fr_{Li}. The energy cost for the neutral state is 4.53 eV per Nb_2O_5 formula, which is 0.65 eV per point defect site, independent to the O- and Nb-rich chemical potential limits. This type of defects has both positive and negative U_{eff} reaction process for charge states variations. For the processes, $2V_{Nb2O5}^{+} \rightarrow V_{Nb2O5}^{0} + V_{Nb2O5}^{2+}$ and $2V_{Nb2O5}^{-} \rightarrow V_{Nb2O5}^{0} + V_{Nb2O5}^{2-}$, they have negative-$U_{eff}$

values of -0.09 eV and -3.38 eV respectively. While the reaction of $2V_{Nb2O5}^{0} \rightarrow V_{Nb2O5}^{2+} + V_{Nb2O5}^{2-}$ shows the positive-U_{eff} value of 3.38 eV. Thus, the 0, +2, and -2 charge states are the most stable charge states within the host lattice across entire band gap sized energetic range. The thermodynamic transition levels for the state (0/2+) and (2-/0) are staying at E_V+1.04 eV and E_V+2.73 eV respectively, showing a deep donor and acceptor behaviors.

Li_2O Schottky defect (V_{Li2O})

The Li_2O vacancy (V_{Li2O}) is also the STK defect. The electronic properties of the resulted under-coordinated Nb- and O- sites are also worth investigating. The TDOS (Figure 9 (a)) shows the neutral V_{Li2O} (V_{Li2O}^{0}) does not contribute any gap states localized within the optical band gap. The V_{Li2O}^{+} defect state only produces one localized hole states next to the CBM with position of E_V+3.77 eV. At the V_{Li2O}^{2+} defect state, two holes states are produced and localized below the CBM (E_V+3.74 eV), and this level are doubly degenerated. For the V_{Li2O}^{-} state, only one localized electronic state is induced within the band gap staying at E_V+2.46 eV. For the V_{Li2O}^{2-} state, there are two localized electronic state staying within the band gap area with positions of E_V+2.40 eV and E_V+2.69 eV. In this case, we find that the V_{Li2O} tends to have doubly degenerated localized electronic and hole states at negatively and positively charged states, respectively.

We further look at the localized orbitals (Figure 9 (b)) regarding different electronic and hole levels induced by different charge states of V_{Li2O} within the host lattice. We see that the all positive charged V_{Li2O} states have nearly the hybridized orbitals between empty Nb-4d and O-2p components with only different orientations within the host lattice. Similarly, all of the negatively charged states of V_{Li2O}, the localized orbitals come from the occupancies of the extra electrons on the Nb-4d orbitals with partial O-2p components staying nearby. Thus, the Nb-4d orbitals within the $LiNbO_3$ host lattice can easily accommodate localized electronic (capture e^-) or hole (release e^-) states.

The formation energy shows the V_{Li2O} does not form as easy as the Fr_{Li} within the lattice (Figure 9 (c)). This arises because the dominant contribution, V_{Li} does not have much energetically favorability to form in the lattice (~2.05 eV at O-rich). Thus, the energy cost to form the neutral V_{Li2O} is 4.44 eV per STK or 1.48 eV per defect site, independent to the variations of chemical potential limits. We also see that, the V_{Li2O} is actually the positive-U_{eff} center and therefore all charge state have relatively long-life time to be stabilized within the host lattice, especially to the energetically distinguishable process, $2V_{Li2O}^{+} \rightarrow V_{Li2O}^{0} + V_{Li2O}^{2+}$.

Full compositional Schottky defect (STK or V_{LiNbO3})

We now consider the full compositional Schottky defect, which is formed by the $LiNbO_3$ vacancy (V_{LiNbO3}). We see from the TDOS (Figure 10 (a)) that the V_{LiNbO3} uniformly produces localized electronic states within the band gap. The neutral state (V_{LiNbO3}^{0}) induces three electronic states nearly degenerated in the band gap with positions of E_V+2.36 eV, E_V+2.38 eV, and E_V+2.47 eV. For its singly positive state (V_{LiNbO3}), one of these electronic states has been ionized and therefore only two are localized in the gap (E_V+2.46 eV and E_V+2.48 eV). The V_{LiNbO3}^{2+} state only produces one localized electronic state staying at E_V+2.46 eV in the gap. For the singly negative charge state (V_{LiNbO3}^{-}), there are three localized electronic states staying slightly deeper in the gap than the ones in V_{LiNbO3}^{0}, which are E_V+2.14 eV, E_V+2.20 eV, and E_V+2.27 eV respectively. For the V_{LiNbO3}^{2-} state, there are

still three electronic states localized within the gap, which are even deeper as E_V+2.04 eV, E_V+2.09 eV, and E_V+2.14 eV respectively.

The localized orbitals of the electronic and hole states induced by V_{LiNbO3} have been investigated (Figure 10 (b)). The V_{LiNbO3} is actually formed up by V_{Li}, V_{Nb} and V_O respectively. We find that these vacancies are closely contacted to each other and this region is electronically active, and the electronic orbitals are localized within this area. The electrons are localized on the on-site Nb-4d orbitals with three-fold symmetrically aligned at the apex points of equivalent triangle area parallel to the plane (0001).

From the energetic view (Figure 10 (c)), the formation energy of the neutral V_{LiNbO3} state is 9.78 eV per STK defect, which is 1.96 eV per defect site, irrespective to the variation of chemical potential limit (O-rich or Nb-rich). This shows the full compositional STK defect is not relatively energetically favorable within the lattice, which is nearly three times higher than the Fr_{Li} and V_{Nb2O5}. This energetic behavior for this STK defect is obviously different from another type of mechanoluminescence solid materials (i.e. CaZnOS), which has been discussed previously by us [83, 84]. The V_{LiNbO3} is a negative-U_{eff} center from the formation energy plot with related to the E_F variation in the gap. The defect reaction process among the change of charge states have the negative-U_{eff}, which are $2V_{LiNbO3}^{0} \rightarrow V_{LiNbO3}^{+} + V_{LiNbO3}^{-}$ and $2V_{LiNbO3}^{0} \rightarrow V_{LiNbO3}^{2+} + V_{LiNbO3}^{2-}$ with values of -1.32 eV and -2.48 eV, respectively. Therefore, the most stable charge states within the host lattice are V_{LiNbO3}^{2+} and V_{LiNbO3}^{2-}.

Native defects induced luminescent properties

(1) Interband transitions via native point or complex defects energy evolutions

Experimentally, both of the mechanoluminescence (ML) and photoluminescence (PL) spectra of the $LiNbO_3:Pr^{3+}$ reported by Xu et al [15], and show three dominant and identical peaks from the range 600 nm ~ 650 nm (609 nm, 619 nm, and 639 nm). The overall PL spectrum centers at 619 nm. The excitation spectra related to this emission PL spectrum are predominantly showing two broad bands centering at 281 nm and 345 nm, which are 4.41 eV and 3.59 eV in photon energy, respectively.

There are two significant factors led us to build the energy transfer model to interpret the ML luminescence property. The first factor is: with the stochiometric ration of Li ($Li_xNbO_3:Pr^{3+}$) decreased, the PL intensity monotonically and vastly decreases with centering peak of 619 nm remained. Meanwhile, as the second factor: the ML spectrum almost matches the one in PL in both peaks positions and overall variation shapes. We therefore deduce that the energies to sustain the ML luminescence are predominantly sourced from the the inter-level transitions by native point defect levels in the host matrix. One of the key channels for this resonant transfer is the Föster resonant energy transfer (FRET). Accordingly, the energy will be resonantly transferred onto the levels of activator center in a continuous way, due to the inter-levels are matching between the ML-activator and PL-activator. Recall, we have previously introduced that the external excitation source is wide-ranged and can accommodate various kinds of excitations in terms of photoirradiation, piezo-electric field, and mechanical forces, etc [83, 84]. From our calculations on the thermodynamic transition levels (TTLs), we find the both electronic and hole transitions along the zero-phonon-line (ZPL) show a variety of matching levels to resonantly transfer the energy onto the ML-activator center. Moreover, the photo-induced electron transfer (PET) is usually active and hopping among different native point defect sites. Thus, the native point defects in luminescent materials play a significant role on determining the luminescence properties, especially for the ML related phosphors. As early as the work down by Wiesendanger et

al[74], the evident inter-band transition has been observed and the low-lying p-d orbital charge transfer related transitions are evident and significant to electrooptic effect.

We summarize these native point defects in the Table S2 and Table S3. Their thermodynamic transitions and single-particle levels have been summarized in Figure 11 (a) and (b). From the theoretical calculation aspect, we have confirmed that there are a variety of inter-level electronic transitions induced energy transfers. Those matching-levels induced single or multi-photon resonance are all potentially responsible for the output emissions of intrinsic mechanoluminescence. As reviewed and summarized by the work of Smyth[85] on the native defects and doping impurities within $LiNbO_3$, it is both highly possible for the coexistence of the n- and p-type electronic states in such insulating piezoelectric materials. This finding actually relies on the relative defect concentration ratios between different charge states and defect species such as excess O (O_i) etc.

These intrinsic electronic/hole inter-level transitions are classified as following paths:

(1) electron-to-electron level transitions, (2) hole-to-hole transitions, (3) electron-to-hole transitions via with n-type charge carriers, (4) hole-to-electron transitions with p-type charge carriers, (5) CBM-to-donor transitions by n-type carriers, (6) VBM-to-acceptor transitions by p-type carriers, and (7) electron-to-VBM transitions. As we previously discussed, the path (3) and (4) are seen to be the most efficiency in releasing the energy since they are mostly have relatively high oscillator strengths [86]. Meanwhile, these two paths are involving the charge alternations process without any change in free energy based on our previously proposed charge alternation pair (CAP) model [87]. Some native point defect complex such as a-Fr_O, Fr_{Nb}, and V_{LiNbO3} are acting as either donor or acceptor like levels.

Regarding the paths in TTLs, for the transition via path (1), the energy is released by the electronic transition between different donor levels, such as $V_O \rightarrow Nb_{Li}$ (636 nm, 627 nm), $V_O \rightarrow Fr_{Li}$ (603 nm, 595 nm), $Li_i \rightarrow Nb_{Li}$ (637 nm), $Nb_i \rightarrow Nb_{Li}$ (608 nm), $Fr_{Nb} \rightarrow V_{Nb2O5}$ (627 nm), $Nb_{Li} \rightarrow Nb_{Li}$ (621 nm) between different levels, respectively. For path (2), the related transitions are given as follows, $V_{Li} \rightarrow V_{Li2O}$ (620 nm), $V_{Nb} \rightarrow Fr_{Li}$ (599 nm), $V_{Nb} \rightarrow V_{Li2O}$ (622 nm), respectively. For the transition via path (3), the transitions are shown as $V_O \rightarrow V_{Nb}$ (603 nm, 595 nm) and a-$Fr \rightarrow V_{Li}$ (623 nm) respectively. For the path (4), the transitions are illustrated as $O_i \rightarrow V_{Nb2O5}$ (618 nm), $Fr_{Li} \rightarrow Fr_{Li}$ (597 nm), $Fr_{Li} \rightarrow Nb_{Li}$ (632 nm), and $V_{Li2O} \rightarrow V_{Li2O}$ (647 nm, 638 nm) respectively. For the path (5), there is no electronic transition from CBM to the donor level responsible for resonantly transfer the energy to the ML center. However, the hole transitions from the $O_i \rightarrow$CBM (626 nm). At the meanwhile, there is also not any hole transition from the VBM to the acceptor level or from the donor level to the VBM by the electron, responsible for the path (6). These classifications have been summarized in the Table S4 accordingly.

As for the SPLs, the electron-lattice coupling effect has been taken into account for the inter-level transitions. The as-classified possible transitions paths have been summarized in the Table 5. There have been found over 194 paths for inter-transitions existing and contributing the three reported PL and ML dominant peaks corresponding to the photon wavelengths of 609 nm, 619 nm, and 639 nm, respectively. Our calculated energetic intervals are converted into the photon energies or wavelengths are in a good agreement with the experimental measurement. In addition, we found that the single native point defects levels are contributing the type-I transition (i.e. path (1)). The mixed transitions which consist of transitions between native point and complex defects (antisite, Frenkel, or Schottky pairs)

levels could be either type-I (path (1)) or IV (path (4)) transitions. The type-I and IV transitions between native pair complex defects levels are also found. However, those Nb-included native Schottky complex defects such as V_{Nb2O5} and V_{LiNbO3} are predominantly contributing the type-IV (hole-type charge carriers) transitions. This arises because the those Nb-related Schottky complex defects are always giving high lying electronic hole states next to the CBM as well as the localized electronic levels staying near the mid-gap. The V_{LiNbO3} defect center sometimes produces the type V and VI transitions, and similar types of transitions have also been found in interstitial Nb_i site. However, the V_{LiNbO3} also gives type VI and VII transitions attributed to their mid-gap localized electronic levels.

On the other hand, the O related anion Frenkel pair (a-Fr_O) complex defects are uniformly contributing the type-I transitions. This is due to the interstitial O_i sites produce the low lying electronic levels localized near the top of the VB. This is also the reason why the O_i acts significantly to be the type-I transition centers as any given electron staying at the level always energetically favors the lower positions within the optical band gap area.

It is also worth mentioning that there is only one O-related inter-level transition contributing the type-IV transition path by hole charge carriers. This arises from the localized hole level below the CB edge by the a-Fr_O pair defects (e.g. a-Fr_O^0, a-Fr_O^+, a-Fr_O^{2+} a-Fr_O^-). Moreover, the O-related a-Fr pair defects possess various local structural configurations due to the O-ion migrations throughout the host lattice, which have been well discussed within rare earth oxides from our previous works[52, 57, 78].

We now start to discuss the inter-level transitions from the aspects of the native defects formation energies. The discussion on formation energies is necessary since the thermodynamic behaviors of the native point defects or complex still exist even under the external high energy irradiation (e.g. UV-light). Then, it has rather high probabilities to further generate the intrinsic defects from the host lattice based on the UV-irradiation. Especially, the experimentally reported excitation energies of UV responsible for both PL and ML luminescence are 4.41 eV and 3.59 eV, which are already reached the level to generate most native point defects or complex according to our above discussion.

Most of the intrinsic defects are formed natively during the process of synthesis, which do not rest on the external excitations. For this case, it is necessary to consider the defect formation at the neutral state. From our early section of discussion, we find that the defect formation energies are asymmetrically distributed between O-poor and O-rich chemical potentials. Under O-poor chemical potential (i.e. Nb-rich in the reducing synthesis atmosphere), the native point defects such as V_O, Nb_i, and Li_i, have relative low formation energies, which are 0.76 eV/site, 0.65 eV/site, and -0.64 eV/site, respectively. The Li_i could be spontaneously formed at this synthesis condition. However, the oxidizing synthesis atmosphere, the formations of native defects cost more energies than the reducing atmosphere. Under O-rich chemical potential (oxidizing atmosphere), the native point defects such as V_{Nb}, V_{Li}, and Li_i, have low formation energies of 2.48 eV, 2.05 eV, and 1.56 eV respectively. Actually, the complex defects actually form independent to the variations of the chemical potentials. We find that the Fr_{Li}, V_{Nb2O5}, and V_{Li2O} also have low formation energies of 0.66 eV/site, 0.65 eV/site, and 1.48 eV/site, respectively.

Except those low-cost intrinsic defects, there are also many intrinsic host defects that can be formed relying on the further external excitation (3.59 eV and 4.41 eV). Meanwhile, these defects are also responsible to involve the PL and ML excitations and emissions. For instance,

the V_O is not the one of such defects since its neutral state has the formation energy of 5.15 eV. The neutral O interstitial defect (O_i) under the O-rich potential limit costs 3.04 eV to form. This indicates the accommodation of the excess O from the ambient under oxidizing condition is capable by 3.59 eV UV irradiation. This type of defect contributes most of the type-I transition paths. The formation of the neutral V_{Nb} site costs energy of 2.48 eV under O-rich and acting as the starting level for the type-IV transitions. For the V_{Li}^0, it has the formation energy of 2.05 eV in O-rich and 4.24 eV in O-poor limit. It seems to be electronically inactive but acting as the core component of forming the Li-complex defects such as V_{Li2O} or Fr_{Li} etc. Moreover, the V_{Li}^0 produces an extra-deep hole trap level next to the CBM acting as the self-quenching centers to annihilate the excited electrons proceeding onto the CB. Thus, this result shows a good agreement with experimental observation that the more V_{Li} concentrations the less intensity of the PL with different excitations wavelengths[15].

Then for the complex, the anion Frenkel pair defect (a-Fr_O) is another typical defect with formation energy of 4.11 eV/site independent to the chemical potentials, which corresponding the UV irradiation with 281 nm (photon energy=4.41 eV). The Fr_{Nb} provides electronic levels within the band gap and its neutral state costs 4.07 eV/site to form the complex. The V_{LiNbO3} contributes high lying electronic states below the conduction band edge, and has the formation energy of 1.96 eV/site at the neutral charge state. The Nb_{Li} defect in neutral state has the formation energy of 2.77 eV per site, which can contribute both type-I and IV transitions.

Combining the Figure 11, Table S4 and S5, we found amount of energy levels from TTLs and SPLs are mostly overlapped. This arises because the energy transfer paths with same or similar energetic intervals are both coming from the single individual and multiple complex centers. Mismatching behavior of the energy levels usually causes depletions of the resonant energy transfer between different energy conversion centers. This will create amount of energy depletion channels once the external mechano-stimulus has been applied on the as-synthesized $LiNbO_3$ sample materials. From our previous work, we found some intrinsic ML and PL materials can have evident extent overlapping in intrinsic host defect levels, which can support substantial amount of resonant energy transfers [83, 84, 87]. On the other hand, as noted from Figure 11 (b), we also found that the hole-to-hole and electron-to-hole transitions are absent when donor-type charge carriers act as energy transfer entities. This arises because the localized holes states are mostly staying near the bottom of the CB edge instead of mid-gap area or near the VB, which are generated by the native point defects or defect complex.

The O-related anion Frenkel pair (a-Fr_O) defects have been reported as the effective entity for the energy conversions [57, 78, 83]. However, in this work, the a-Fr_O is not energetically preferred to forming in the host and playing as the energy conversion center. On the other hand, it is worth considering whether the Nb-4d crystal field splitting (CFS) effect is evident to impact the electronic structure. As we know, the 4d orbital CFS effect is usually stronger than the ones in 3d orbitals (i.e. 4d>3d). However, the Nb-4d ($4d^45s^1 \leftrightarrow 4d^55s^0$) orbitals can be occupied by the 5 d-electrons with 2 electrons on the $4d_{eg}$ and 3 electrons on the $4d_{t2g}$ levels in the high-spin state configuration. Our estimation shows either octahedral or tetrahedral ligand field configuration returns the crystal field stabilization energy (CFSE) uniformly the zero. Accordingly, there is no substantial impact on the electronic structures by the CFS effect from Nb-4d orbitals.

(2) Thermodynamic energy evolutions via the native point and complex defects

We further found that the agglomerating (aggregating) effect is strongly favorable in physicochemical trend, since the formation energy calculations tell that the system energetically favors the formation of the complex defects. Such agglomerating effect is the equilibrium process to form the native complex defects within the host matrix via the aggregations or close contact of the separately distributed individual single point defects (as constituents). We found that the effective agglomerating effect favors more in energetics than those separated individuals. However, the a-Fr_O is found to be an exceptions here in this work. The a-Fr_O shows unfavorable to form within the host, since it neither gains energy from the agglomerating effect from the (V_O+O_i) nor has an obvious energetic contrast before or after the agglomerating effect.

We have summarized the change in free energy under such equilibrium transition process to energetically describe the defects migrations and agglomerating effect as shown in Table 1. With supported by Table S3, the original formation energies of some neutral native complex defects are high while the others are very low.

However, they almost show that there are two processes are rather energetically favorable: (1) The charge alternation transition from the neutral separate individual point defects to the complementarily charged individual point defects; (2) The agglomeration from the complementarily charged separate individual point defects to the aggregated (or closely contacted) native complex defects. Moreover, we found that the energy gains from the electronically active point defects to the complex defects are actually a generalized phenomenon. The energy gain for both two processes turns to be independent to the variations of the O or Nb chemical potentials. As we can see from the Table 6 that, the energy is almost the same for both O-rich and Nb-rich chemical potential limits. Such generalized energy gain can be achieved by the local lattice relaxations, which follows the physical trend of electron-lattice coupling effect[87].

Previously, we have studied the energy harvesting and conversions for the ML applications for the CaZnOS system [83, 84]. The native point defect levels have been extensively discussed and interpreted in terms of the thermodynamic transition level and single particle levels. From that work, we finally screened the candidates as electronic active centers for the ML energy transfers, which are V_{ZnO} and V_{CaZnOS} respectively. Meanwhile, the a-Fr_O and a-Fr_S are also energy kinetically favorable to proceed the dynamic energy transport. Herein, combining with our energy conversion model, we confirm that the V_{ZnO} and V_{CaZnOS} are the energetically significant to support the energy transfer in the ML, which is once again verified from our more generalized theoretical mechanism, with much evident solid consistency shown in Figure 11 (c).

Further looking at the Figure 11 (c), we find that the V_{Nb2O5} has the largest agglomerated energy stabilization. The antisite Nb_{Li} possesses the second largest stabilization energy from the agglomeration process, and the V_{LiNbO3} is the third. The V_{Li2O} shows almost zero agglomeration energetic gain which means a reversible process in a nearly zero structural configuration entropy transition. However, both of the a-Fr_O and Fr_{Li} cases show an endothermic effect for agglomeration, which are energetically unfavorable or electronically inert to participate in the ML energy transfer. This case is rather different from the one we found in CaZnOS system [83, 84]. Previous studies by both Li et al[69] and Marsh et al[35] have addressed the significance of the Nb_{Li} in the interband transitions to influence the optical absorption measurement. Here our work not only confirms this important conclusion

but also more insightfully found the existence of the V_{Nb2O5} and its role in energy transfer for self-recoverable ML process.

The energy released from the relaxation of the electron-lattice coupling can resonant the energy to match the electronic transitions intervals between the different levels localizing at the nearby intrinsic defect regions. This non-radiative resonant energy can be further transfer throughout the lattice with much less impact by the phonon participation, since the electronic-lattice coupling effect for complementarily charged point defects relaxation has already been counteracted to each other. Therefore, these energy gains from the neutral to the complementarily charged and further transform into the agglomeration can be seen as a type of FRET-like (Föster resonant energy transfer) to transfer the energy without the influence to the local lattice distortion to transfer the energy non-radiatively and sustain with a substantially long distance, to support the single or multi-photon process of electronic transitions. Thus, we have the following equations with considerations of the three different types of photons with energies of 2.04 eV (609 nm), 2.00 eV (619 nm), and 1.94 eV (639 nm) respectively:

$$\Delta E_{form}(x, y, z) = xE_1 + yE_2 + zE_3 \tag{5}$$

From the Eq (5), the E_1, E_2, and E_3 represent the three typical photon energies (E_1=2.04 eV, E_2=2.00 eV, E_3=1.94 eV), where the (x, y, z) determines the numbers of photons corresponding to the given photon energy. We note that, the less degree to distinguish the E_1, E_2, and E_3, the broader the peaks for the PL or ML emission spectrum will be observed from the experiment. Therefore, the Eq (5) turns out to be the multiple valued functions and non-monotonically varied by the variables. We take the example from the native complex defects, the antisite Nb_{Li} defect, from the Table 1. Both energy gains from the process (1) (charged) or process (2) (agglomerated) are shown as -6.06 eV and -6.10 eV. The magnitude of the energies can be seen as all three photons participated or partially participated as follows:

$$\begin{cases} (x=1, y=1, z=1) \\ (x=3, y=0, z=0) \\ (x=0, y=3, z=0) \\ (x=1, y=2, z=0) \\ (x=2, y=1, z=0) \end{cases} \tag{6}$$

As we know, the energy cost for forming the Nb_{Li} can be seen as still relatively high compared with the most comment V_O defects in the host. However, Table 1 shows that the absolute value of the energy gain from equilibrium transition in either charged or agglomerated process are both larger than the neutral formation energy of the Nb_{Li} in the host lattice. Therefore, such formation activation barrier can be overcome by the local lattice relaxations nearby native point defects.

On the other hand, the V_{Nb2O5} are showing the energy gains for the two processes are -10.00 eV and -16.18 eV. These energies can be evidently support the resonanting the electronic transitions for emitting te short wavelength photons, which can be (x=0, y=5, z=0) and (x=8, y=0, z=0), respectively. Therefore, the energy support for the electronic transitions that sustains for a long distance within the host and long durations with long life-time decay can be predominantly contributed by the Nb_{Li} and V_{Nb2O5} synergistically onto the V_{LiNbO3} site

as shown in Figure 11 (d). Based on discussions, it is found that in the both energetics and electronics, there has no advantage for the native point defects to the native complex defects. According to the chemical potential boundaries (Figure 2), it shows that the native complex defects are more energetically favorable to the point defects.

We move onto the modeling the change in free energy if we do not consider temperature variation effects as well as the zero-point vibration energies for each defects. Then, with conversing the energy variations of *charged* and *agglomerated* from the Table 1, the mechanical loading (ML) as well as the ML loading cycles can be simplified in the energy changing pathways (Figure 11 (e)). By using these pathways, we can clearly see the both individual contributions and collective physicochemical trend on how to harvest and transfer the energy with different magnitude of loading of external mechanical excitations. From Figure 11 (e), we found even the intrinsic un-doped $LiNbO_3$ system can clearly reflect the energy trapping centers given by the oxygen anion Frenkel pair defects (a-Fr_O), which requires a pre-stimulation by the UV light. Also, with existence of this energy trap, the emission intensity and reversibility are found to be decreased with ML-loading cycles increasing. This finding shows a good agreement with experimental observation by Xu et al[15]. We also exhibit the energy changing pathway in the system of previous discussed CaZnOS [83, 84] and further confirmed the mechanical quenching effect that reported previously by Xu et al[5, 14].

Conclusion

We have studied the native point defect levels of $LiNbO_3$ to interpret the intrinsic mechanoluminescence mechanism. We found the both interstitial and vacancy defects are low energy defects, and mutually interplay through series of defect chemical reactions for energy transfer between different charge states from the host. Moreover, the formations of native defects under the oxidizing synthesis atmosphere cost more energies than the reducing atmosphere. Under O-poor chemical potential (i.e. Nb-rich in the reducing synthesis atmosphere), the V_O, Nb_i, and Li_i, have relative low formation energies, which are 0.76 eV/site, 0.65 eV/site, and -0.64 eV/site, respectively. The Li_i is found to be spontaneously formed at this synthesis condition. In addition, the complex defects actually form independent to the variations of the chemical potentials. We find that the Fr_{Li}, V_{Nb2O5}, and V_{Li2O} also have low formation energies of 0.66 eV/site, 0.65 eV/site, and 1.48 eV/site, respectively. We also predict the energy transfer cycle paths along the zero-phonon lines responsible for the intrinsic persistent luminescence, which is the $V_{Nb2O5} \rightarrow O_i$, the charge balance can be achieved by the Li_i^+ and V_O^{2+} since these native defects have negative formation energy and can be spontaneously formed and transporting with energetic barriers free throughout the host lattice. Therefore, in defect reaction related energy conversion, both interstitials and vacancies are the native activators sites to accommodate the recombination of the excited electrons and holes and release the energy by photon emission.

Acknowledgement

The author gratefully acknowledges the support of the Natural Science Foundation of China (NSFC) for the Youth Scientist grant (Grant No.: NSFC 11504309, 21771156), the initial start-up grant support from the Department General Research Fund (Dept. GRF) from ABCT in the Hong Kong Polytechnic University, and the Early Career Scheme (ECS) fund (Grant No.: PolyU 253026/16P) from the Research Grant Council (RGC) in Hong Kong.

Table 1. Summary of the free energy gains for the formation of the native complex defects. The change in formation energies are shown for the two process: (1) from the neutral separate individuals to the complementarily charged separate individuals (i.e. "Charged" in the table); (2) from the complementarily charged separate individuals to the neutral agglomerated complex (i.e. "Agglomerated" in the table). The NbLi* denotes an indirect transfer from $(V_{Li}+Li_i)+(V_{Nb}+Nb_i)$.

Complex	O-rich		Nb-rich	
	Charged	Agglomerated	Charged	Agglomerated
V_{LiNbO3}	-7.37	-2.83	-7.37	-2.81
V_{Nb2O5}	-10.00	-16.18	-10.00	-16.15
V_{Li2O}	-4.74	-0.07	-4.74	-0.06
a-Fr_O	-2.22	2.25	-2.23	2.26
Fr_{Li}	-2.54	0.24	-2.53	0.24
Fr_{Nb}	-3.52	-2.45	-3.52	-2.44
Nb_{Li}	-6.06	-6.10	-6.05	-6.09
Nb_{Li}*	-3.89		-3.89	

Figure 1.

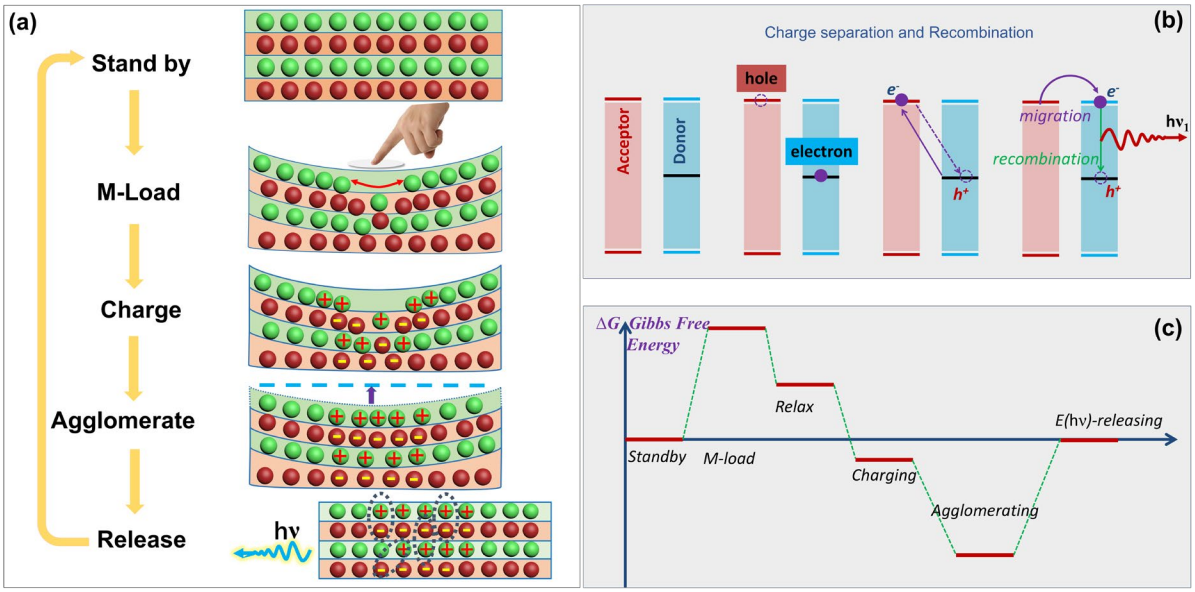

Figure 1. Schematic illustrating diagram about the native defects induced energy harvesting and conversion model for the elastic mechano-persistent luminescence (self-recoverable). (a) Microscopic view on the atomic and electronic mechanisms for the elastic-ML. (b) The schematic energy diagrams for the energy transfer and charge transitions for piezoelectric ML. (c) The overall systematic Gibbs free energy (ΔG) diagram for illustrating the energetics on the self-recoverable ML mechanism.

Figure 2.

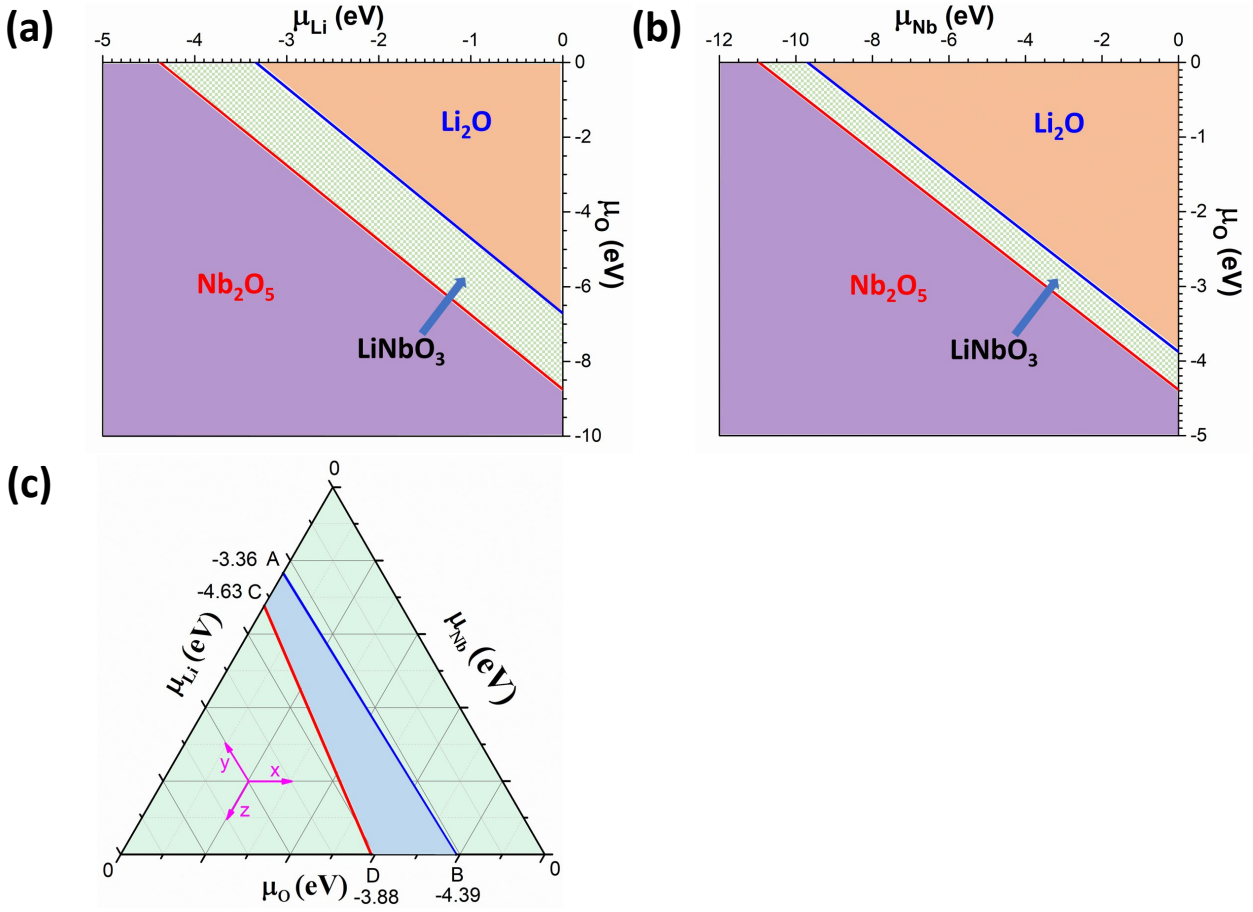

Figure 2. Calculated phase diagrams with respect to chemical potentials of Li (μ_{Li}), Nb (μ_{Nb}), and O (μ_O) elements.

Figure 3.

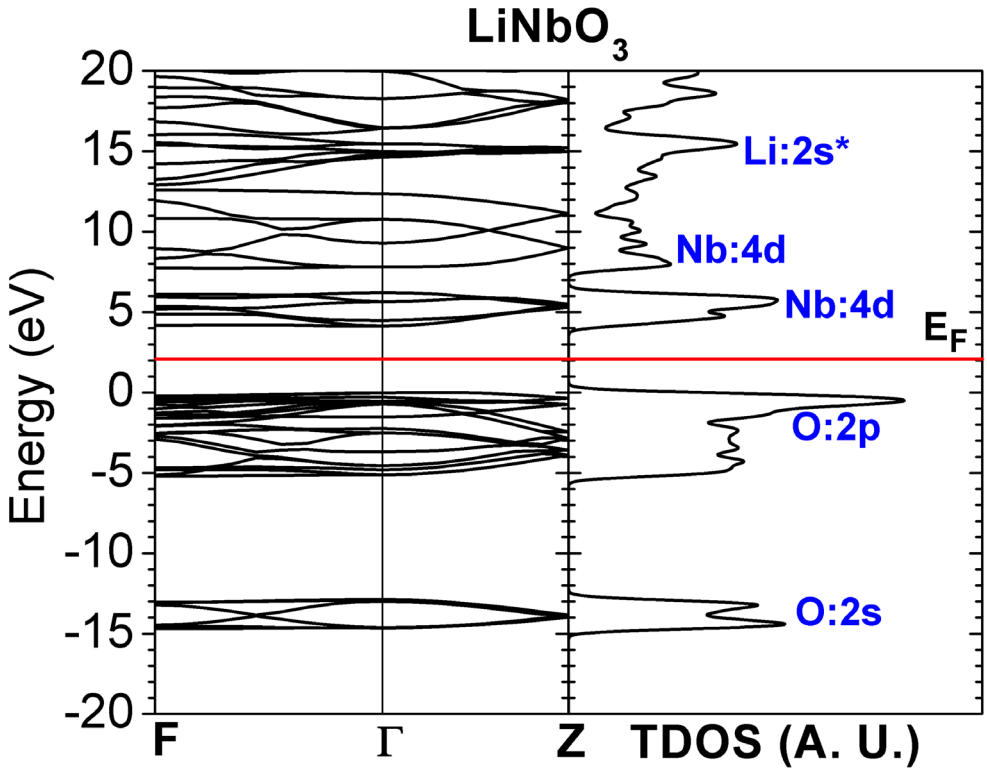

Figure 3. Band structure and total density of states (TDOSs) of $LiNbO_3$.

Figure 4.

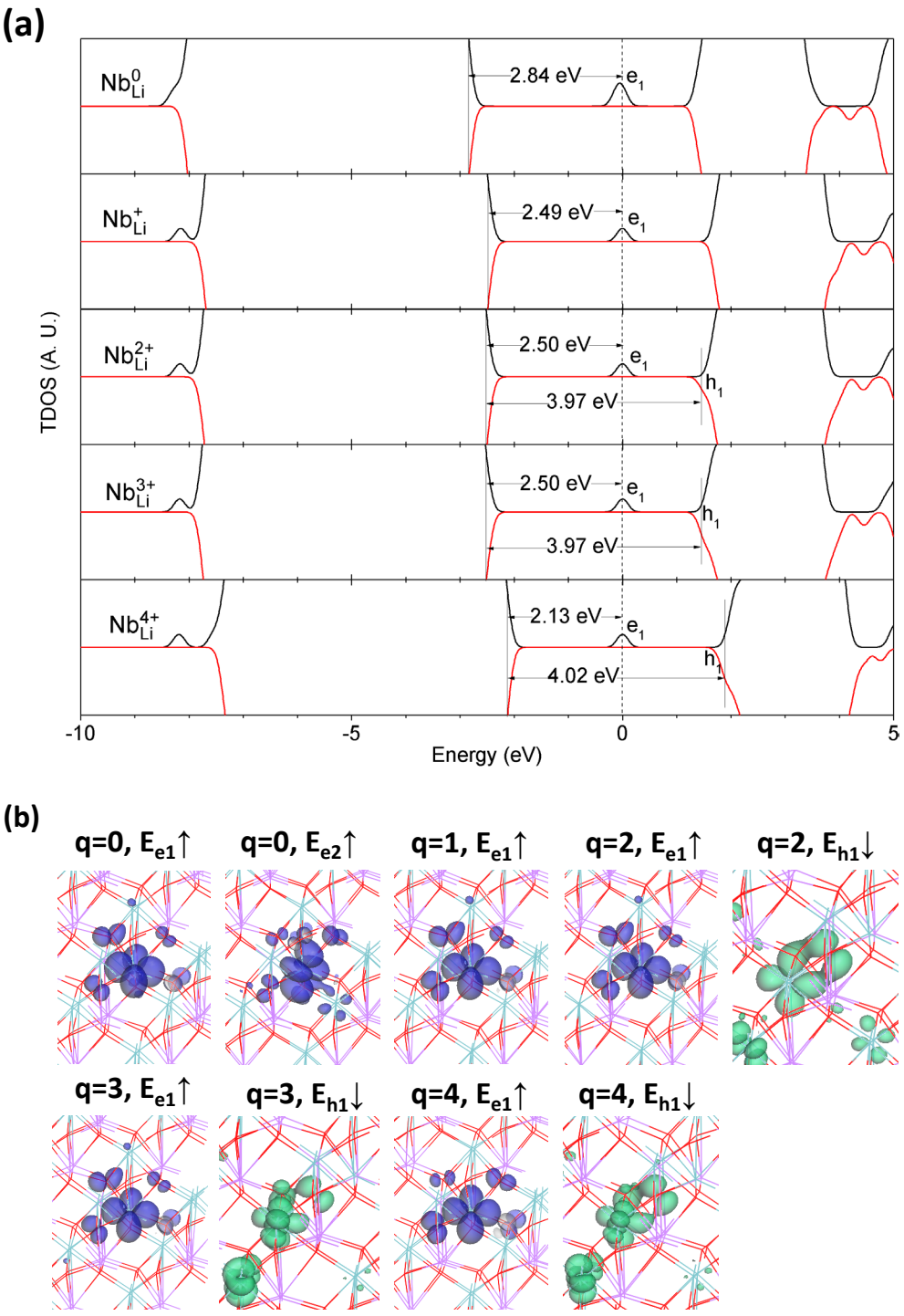
(a)
Nb^{0}_{Li}
Nb^{+}_{Li}
Nb^{2+}_{Li}
Nb^{3+}_{Li}
Nb^{4+}_{Li}
2.84 eV
2.49 eV
2.50 eV
3.97 eV
2.50 eV
3.97 eV
2.13 eV
4.02 eV
e_1
h_1
TDOS (A. U.)
-10
-5
0
5
Energy (eV)
(b)
q=0, E_{e1}↑
q=0, E_{e2}↑
q=1, E_{e1}↑
q=2, E_{e1}↑
q=2, E_{h1}↓
q=3, E_{e1}↑
q=3, E_{h1}↓
q=4, E_{e1}↑
q=4, E_{h1}↓

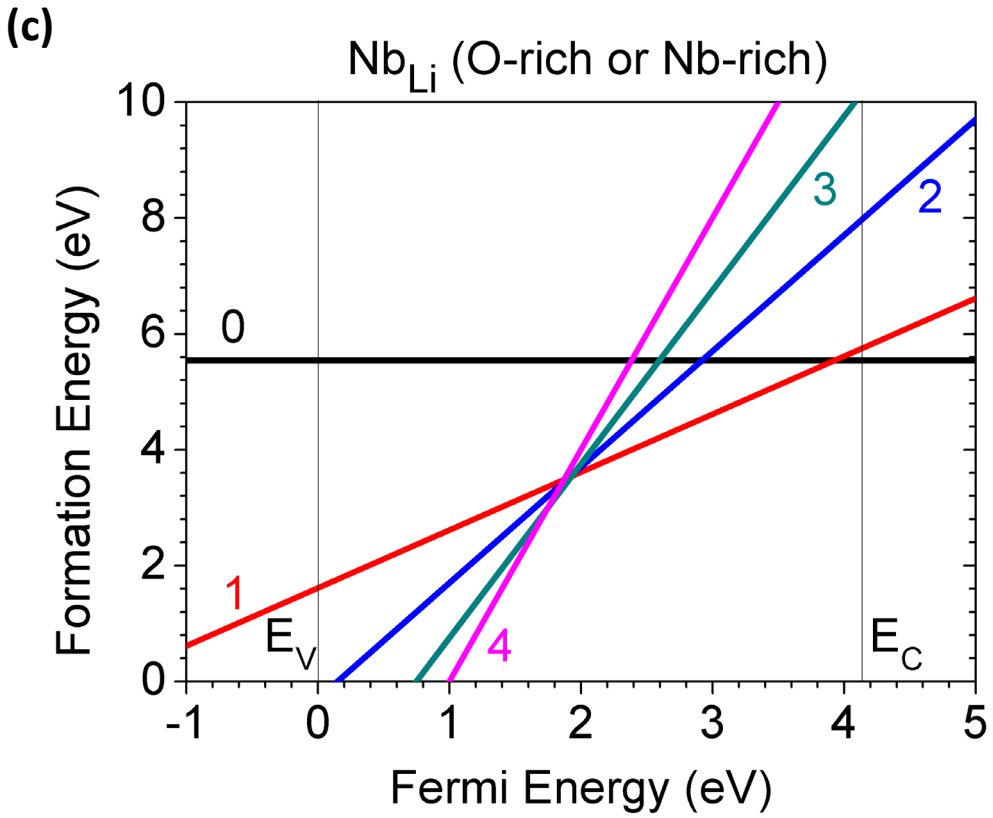

Figure 4. (a) TDOSs of Nb_{Li} in neutral (Nb_{Li}^{0}), singly negative (Nb_{Li}^{+}), doubly negative (Nb_{Li}^{2+}), triply negative (Nb_{Li}^{3+}), and quadruply negative (Nb_{Li}^{4+}). The dashed line denotes the highest occupied level for electrons. (b) Localized electron and hole orbitals at the relaxed Nb_{Li} site with side views (Li=purple, O=red, Nb=cyan). (c) Formation energies of Nb_{Li} under O- or Nb- rich chemical potential limits.

Figure 5.

(a)

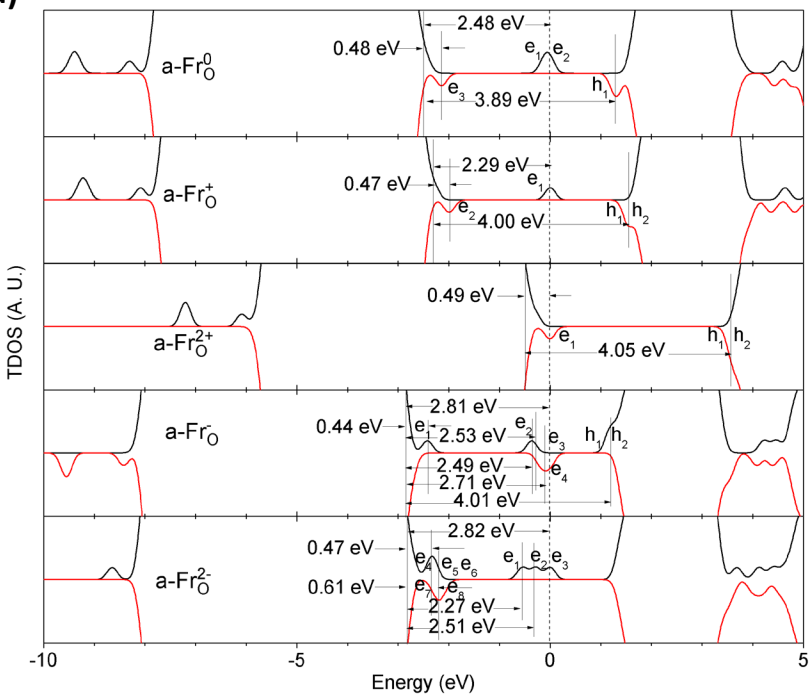
a-Fr$_O^0$
2.48 eV
0.48 eV
e$_1$ e$_2$
e$_3$ 3.89 eV
h$_1$
a-Fr$_O^+$
2.29 eV
0.47 eV
e$_1$
e$_2$ 4.00 eV
h$_1$ h$_2$
a-Fr$_O^{2+}$
0.49 eV
e$_1$ 4.05 eV
h$_1$ h$_2$
a-Fr$_O^-$
2.81 eV
0.44 eV
e$_1$ 2.53 eV e$_2$ e$_3$
h$_1$ h$_2$
2.49 eV
2.71 eV
e$_4$
4.01 eV
a-Fr$_O^{2-}$
2.82 eV
0.47 eV
e$_4$ e$_5$ e$_6$
e$_1$ e$_2$ e$_3$
0.61 eV
e$_7$ e$_8$
2.27 eV
2.51 eV
TDOS (A. U.)
-10
-5
0
5
Energy (eV)

(b)

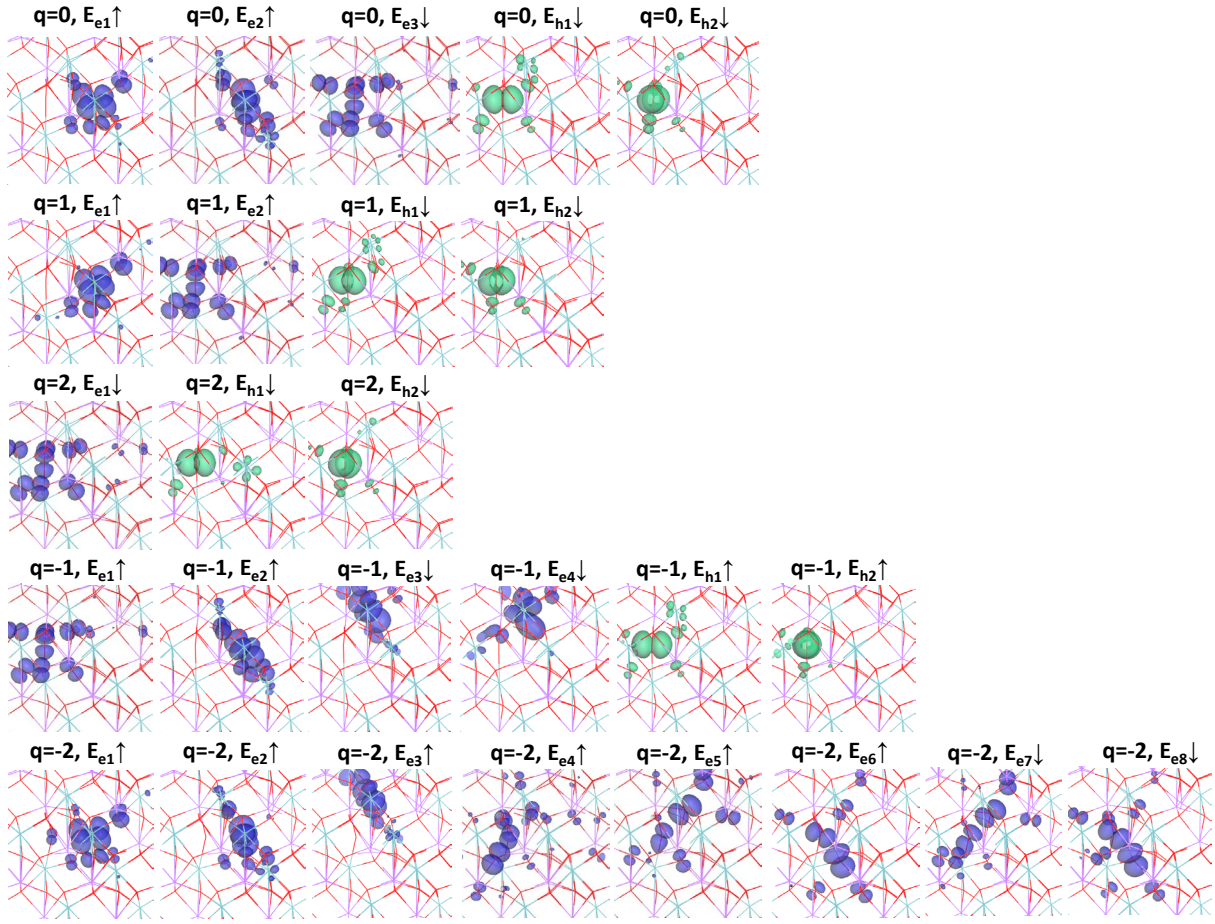
q=0, E$_{e1}$↑
q=0, E$_{e2}$↑
q=0, E$_{e3}$↓
q=0, E$_{h1}$↓
q=0, E$_{h2}$↓
q=1, E$_{e1}$↑
q=1, E$_{e2}$↑
q=1, E$_{h1}$↓
q=1, E$_{h2}$↓
q=2, E$_{e1}$↓
q=2, E$_{h1}$↓
q=2, E$_{h2}$↓
q=-1, E$_{e1}$↑
q=-1, E$_{e2}$↑
q=-1, E$_{e3}$↓
q=-1, E$_{e4}$↓
q=-1, E$_{h1}$↑
q=-1, E$_{h2}$↑
q=-2, E$_{e1}$↑
q=-2, E$_{e2}$↑
q=-2, E$_{e3}$↑
q=-2, E$_{e4}$↑
q=-2, E$_{e5}$↑
q=-2, E$_{e6}$↑
q=-2, E$_{e7}$↓
q=-2, E$_{e8}$↓

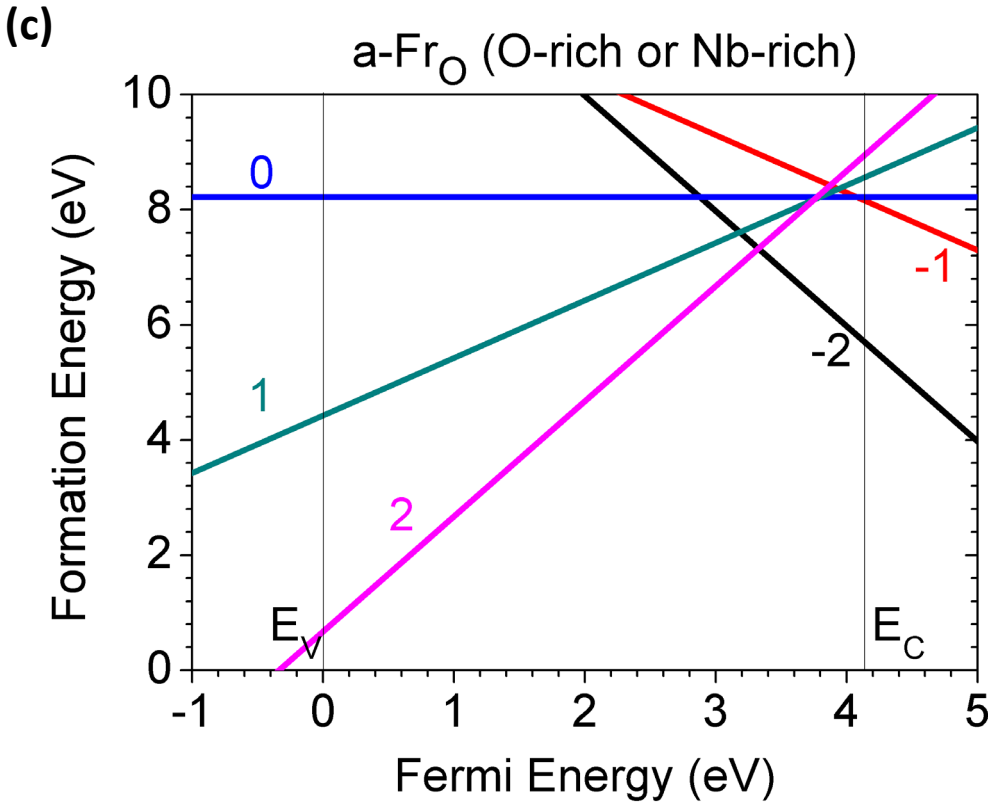

Figure 5. (a) TDOSs of a-Fr in neutral (a-Fr^0), singly positive (a-Fr$^+$), doubly positive (a-Fr^{2+}), singly negative (a-Fr$^-$), and doubly negative (a-Fr^{2-}). The dashed line denotes the highest occupied level for electrons. (b) Localized electron and hole orbitals at the relaxed a-Fr site with side views (Li=purple, O=red, Nb=cyan). (c) Formation energies of a-Fr under O- or Nb- rich chemical potential limits.

Figure 6.

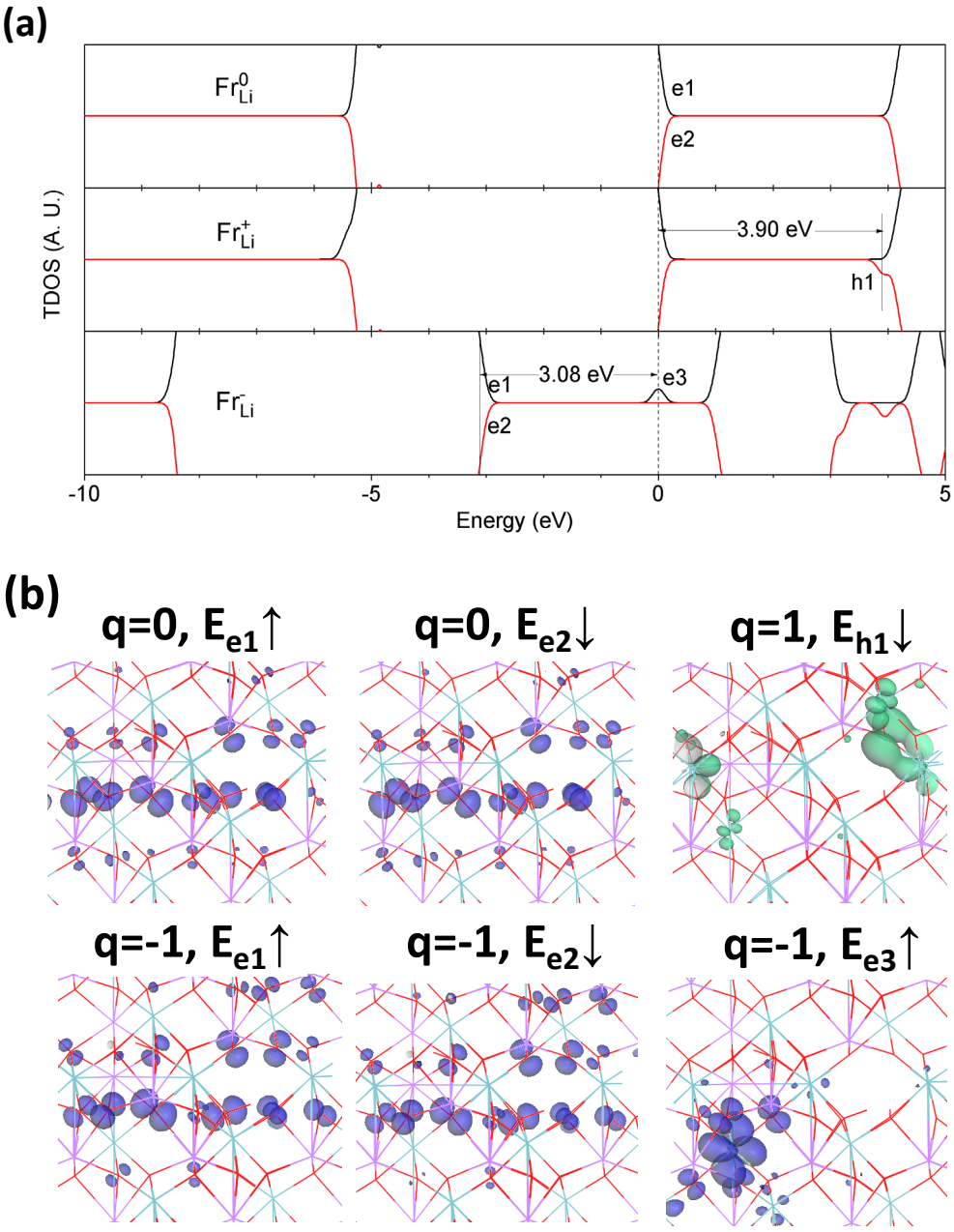
(a)
Fr^{0}_{Li}
e1
e2
Fr^{+}_{Li}
3.90 eV
h1
Fr^{-}_{Li}
e1
3.08 eV
e3
e2
TDOS (A. U.)
-10
-5
0
5
Energy (eV)
(b)
q=0, E_{e1}↑
q=0, E_{e2}↓
q=1, E_{h1}↓
q=-1, E_{e1}↑
q=-1, E_{e2}↓
q=-1, E_{e3}↑

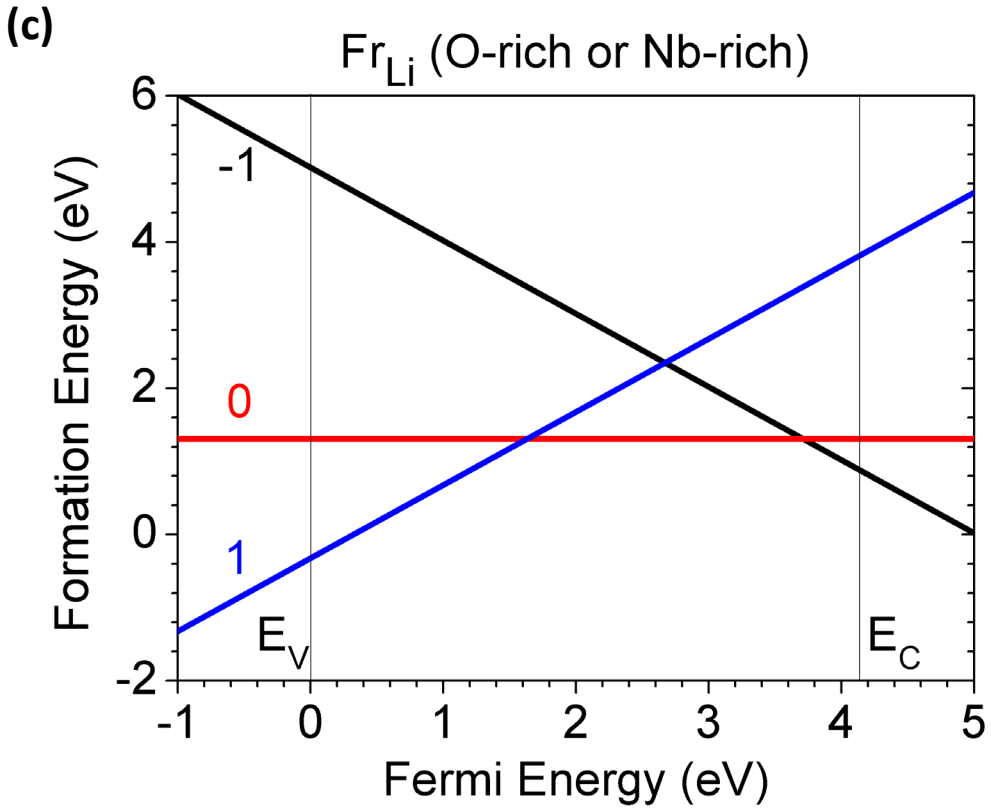

Figure 6. (a) TDOSs of Fr_{Li} in charge states of 0, +1, and -1. The dashed line denotes the highest occupied level for electrons. (b) Localized electron and hole orbitals at the relaxed Fr_{Li} site with side views (Li=purple, O=red, Nb=cyan). (c) Formation energies of Fr_{Li} under O- or Nb- rich chemical potential limits.

Figure 7.

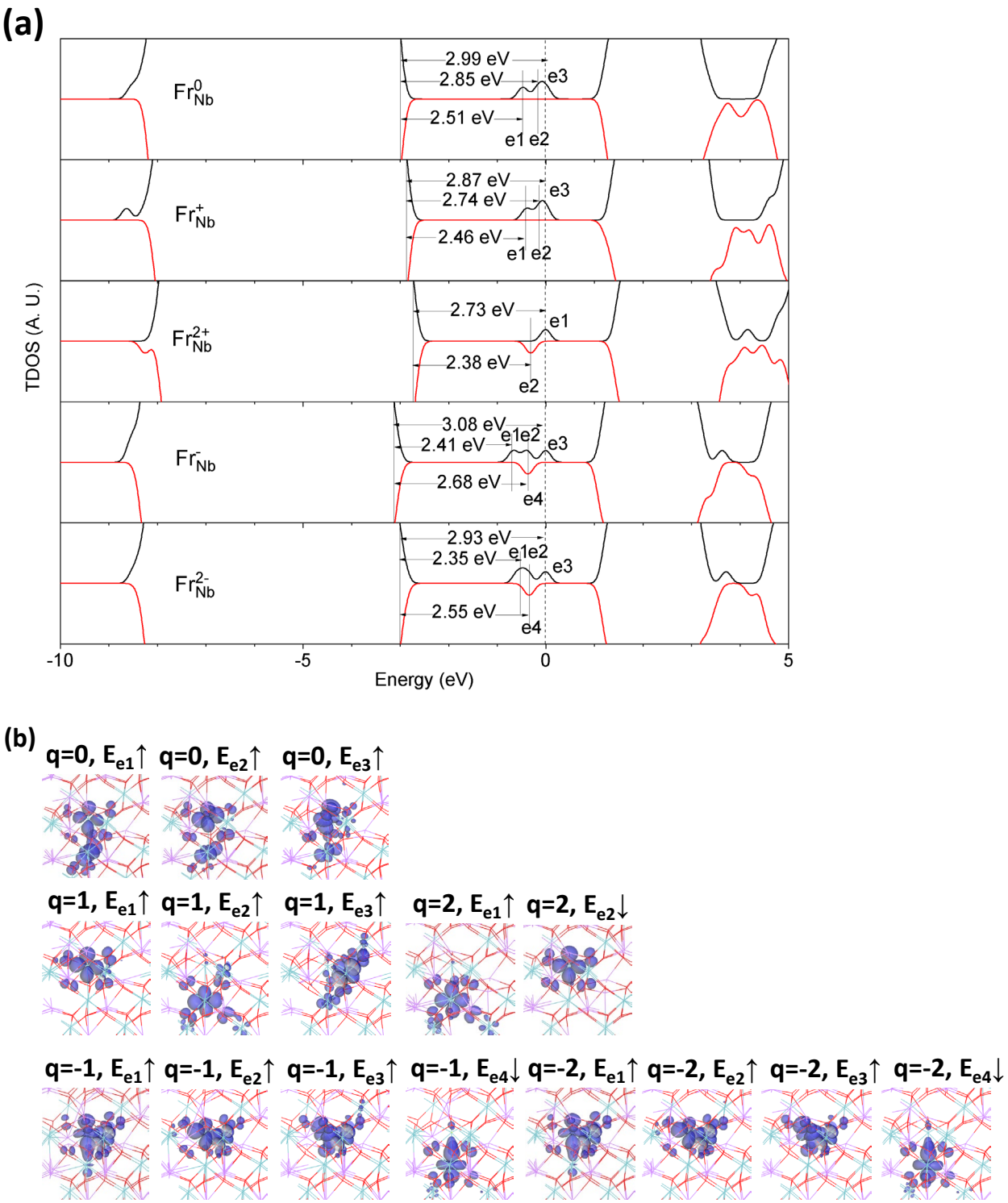
(a)
Fr^{0}_{Nb}
2.99 eV
2.85 eV
e3
2.51 eV
e1 e2
Fr^{+}_{Nb}
2.87 eV
2.74 eV
e3
2.46 eV
e1 e2
Fr^{2+}_{Nb}
2.73 eV
e1
2.38 eV
e2
Fr^{-}_{Nb}
3.08 eV
2.41 eV
e1e2
e3
2.68 eV
e4
Fr^{2-}_{Nb}
2.93 eV
2.35 eV
e1e2
e3
2.55 eV
e4
TDOS (A. U.)
-10
-5
0
5
Energy (eV)
(b)
q=0, $E_{e1}\uparrow$
q=0, $E_{e2}\uparrow$
q=0, $E_{e3}\uparrow$
q=1, $E_{e1}\uparrow$
q=1, $E_{e2}\uparrow$
q=1, $E_{e3}\uparrow$
q=2, $E_{e1}\uparrow$
q=2, $E_{e2}\downarrow$
q=-1, $E_{e1}\uparrow$
q=-1, $E_{e2}\uparrow$
q=-1, $E_{e3}\uparrow$
q=-1, $E_{e4}\downarrow$
q=-2, $E_{e1}\uparrow$
q=-2, $E_{e2}\uparrow$
q=-2, $E_{e3}\uparrow$
q=-2, $E_{e4}\downarrow$

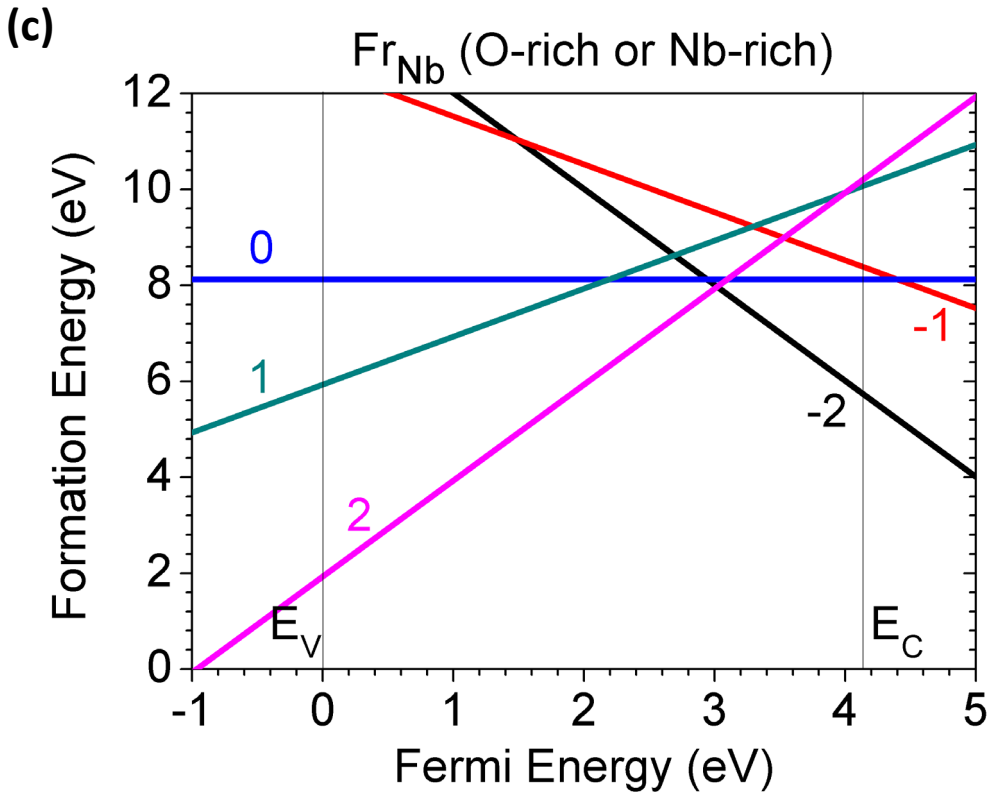

Figure 7. (a) TDOSs of Fr_{Nb} in neutral (Fr_{Nb}^{0}), singly positive (Fr_{Nb}^{+}), doubly positive (Fr_{Nb}^{2+}), singly negative (Fr_{Nb}^{-}), and doubly negative (Fr_{Nb}^{2-}). The dashed line denotes the highest occupied level for electrons. (b) Localized electron and hole orbitals at the relaxed Fr_{Nb} site with side views (Li=purple, O=red, Nb=cyan). (c) Formation energies of Fr_{Nb} under O- or Nb- rich chemical potential limits.

Figure 8.

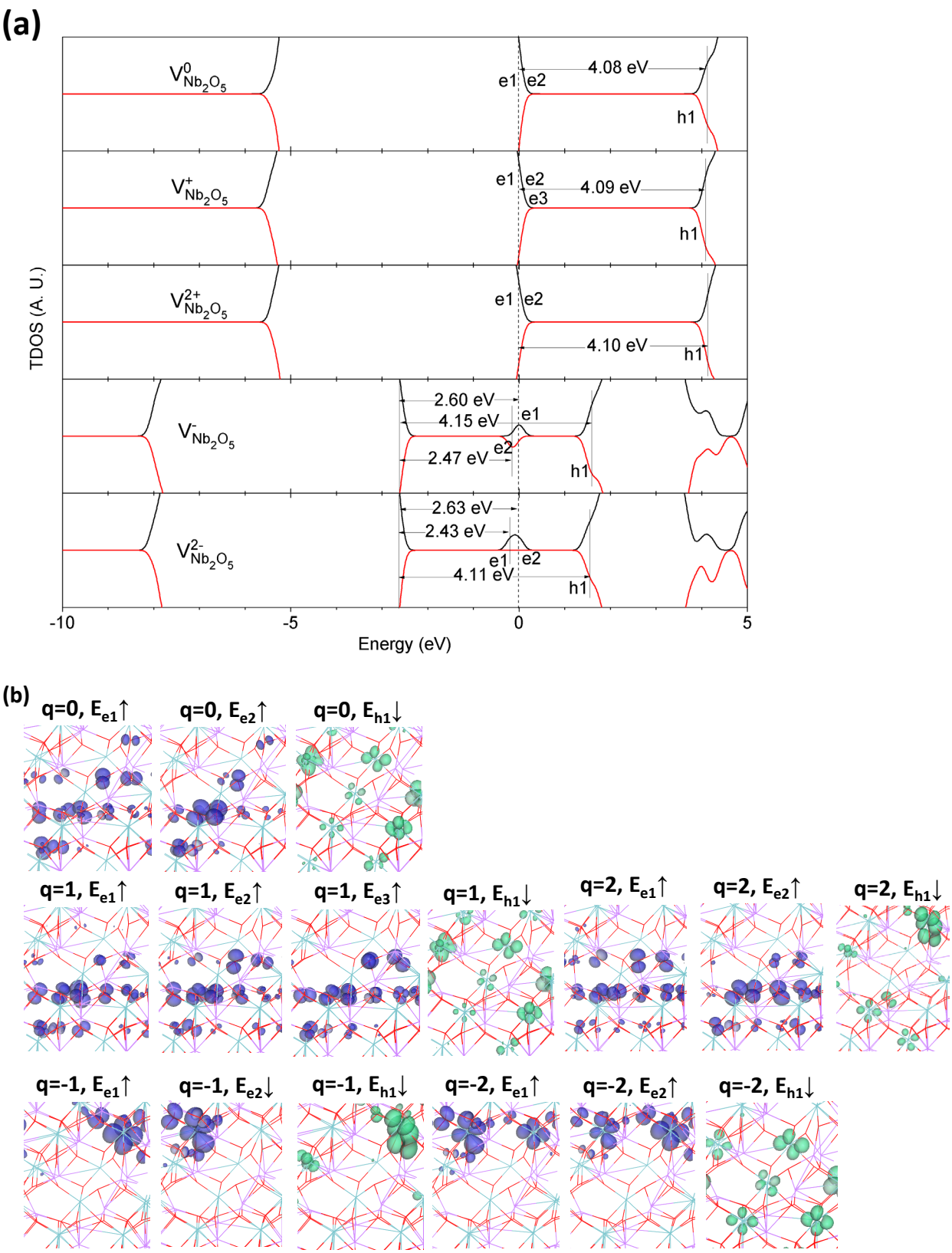
(a)
$V^{0}_{Nb_2O_5}$
$V^{+}_{Nb_2O_5}$
$V^{2+}_{Nb_2O_5}$
$V^{-}_{Nb_2O_5}$
$V^{2-}_{Nb_2O_5}$
e1
e2
e3
h1
4.08 eV
4.09 eV
4.10 eV
2.60 eV
4.15 eV
2.47 eV
2.63 eV
2.43 eV
4.11 eV
TDOS (A. U.)
-10
-5
0
5
Energy (eV)
(b)
q=0, $E_{e1}\uparrow$
q=0, $E_{e2}\uparrow$
q=0, $E_{h1}\downarrow$
q=1, $E_{e1}\uparrow$
q=1, $E_{e2}\uparrow$
q=1, $E_{e3}\uparrow$
q=1, $E_{h1}\downarrow$
q=2, $E_{e1}\uparrow$
q=2, $E_{e2}\uparrow$
q=2, $E_{h1}\downarrow$
q=-1, $E_{e1}\uparrow$
q=-1, $E_{e2}\downarrow$
q=-1, $E_{h1}\downarrow$
q=-2, $E_{e1}\uparrow$
q=-2, $E_{e2}\uparrow$
q=-2, $E_{h1}\downarrow$

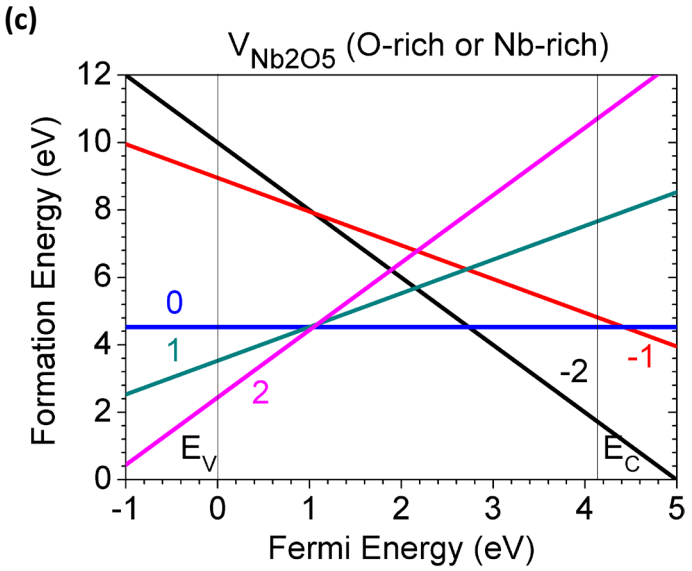

Figure 8. (a) TDOSs of V_{Nb2O5} in charge states of 0, +1, -1, +2, and -2. The dashed line denotes the highest occupied level for electrons. (b) Localized electron and hole orbitals at the relaxed V_{Nb2O5} site (Li=purple, O=red, Nb=cyan). (c) Formation energies of V_{Nb2O5} under O- or Nb- rich chemical potential limits.

Figure 9.

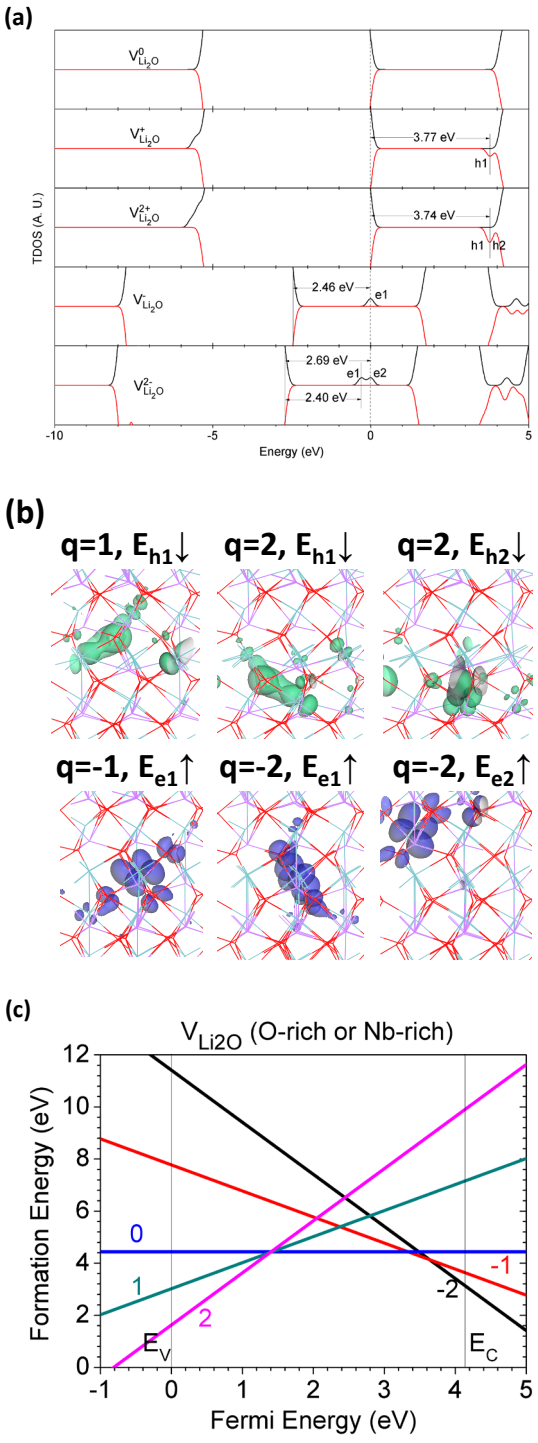

Figure 9. (a) TDOSs of V_{Li2O} in charge states of 0, +1, -1, +2, and -2. The dashed line denotes the highest occupied level for electrons. (b) Localized electron and hole orbitals at the relaxed V_{Li2O} site (Li=purple, O=red, Nb=cyan). (c) Formation energies of V_{Li2O} under O- or Nb- rich chemical potential limits.

Figure 10.

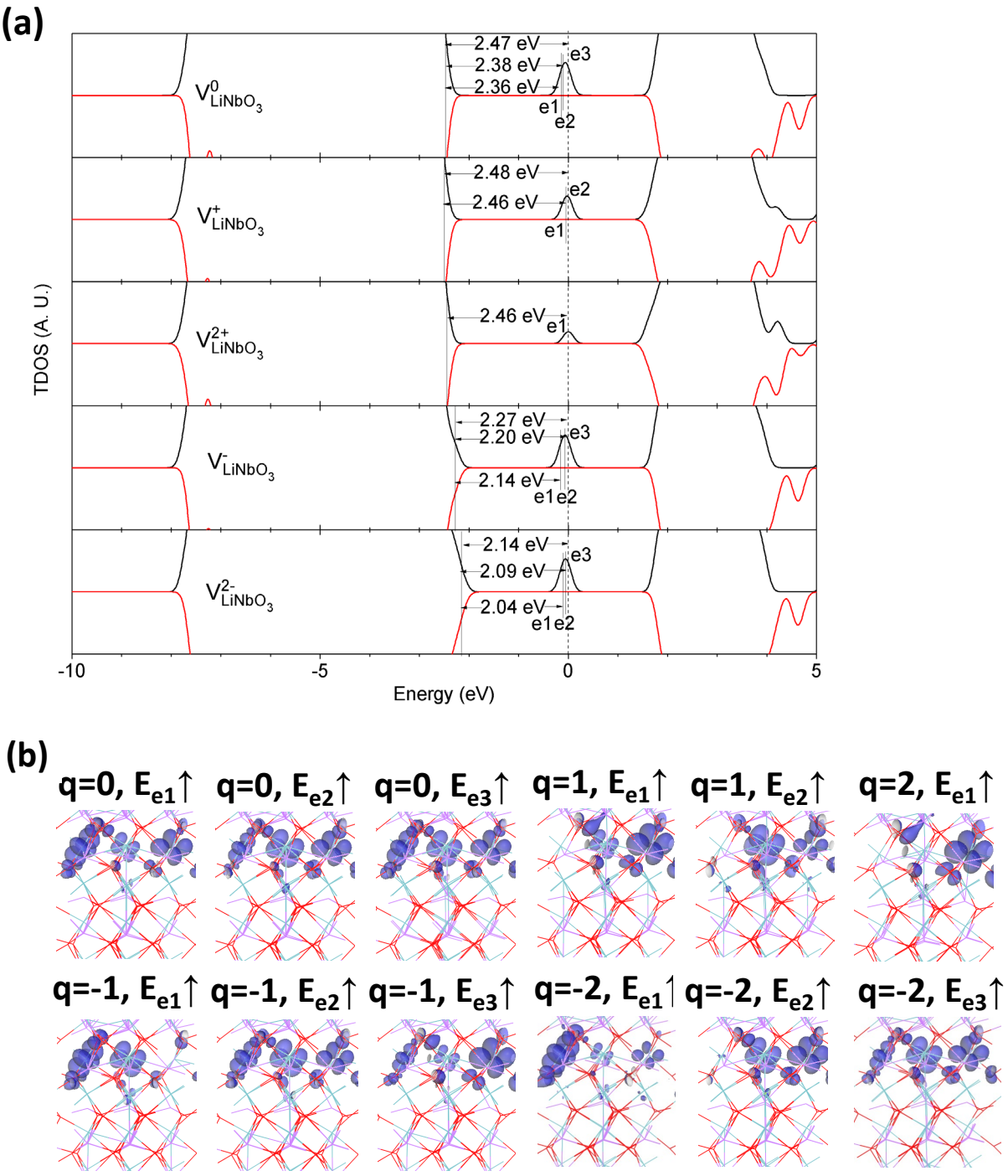
(a)
2.47 eV
2.38 eV
2.36 eV
e3
e1
e2
$V^{0}_{LiNbO_3}$
2.48 eV
2.46 eV
e2
e1
$V^{+}_{LiNbO_3}$
2.46 eV
e1
$V^{2+}_{LiNbO_3}$
2.27 eV
2.20 eV
e3
2.14 eV
e1e2
$V^{-}_{LiNbO_3}$
2.14 eV
2.09 eV
e3
2.04 eV
e1e2
$V^{2-}_{LiNbO_3}$
TDOS (A. U.)
-10
-5
0
5
Energy (eV)
(b)
q=0, E_{e1}↑
q=0, E_{e2}↑
q=0, E_{e3}↑
q=1, E_{e1}↑
q=1, E_{e2}↑
q=2, E_{e1}↑
q=-1, E_{e1}↑
q=-1, E_{e2}↑
q=-1, E_{e3}↑
q=-2, E_{e1}↑
q=-2, E_{e2}↑
q=-2, E_{e3}↑

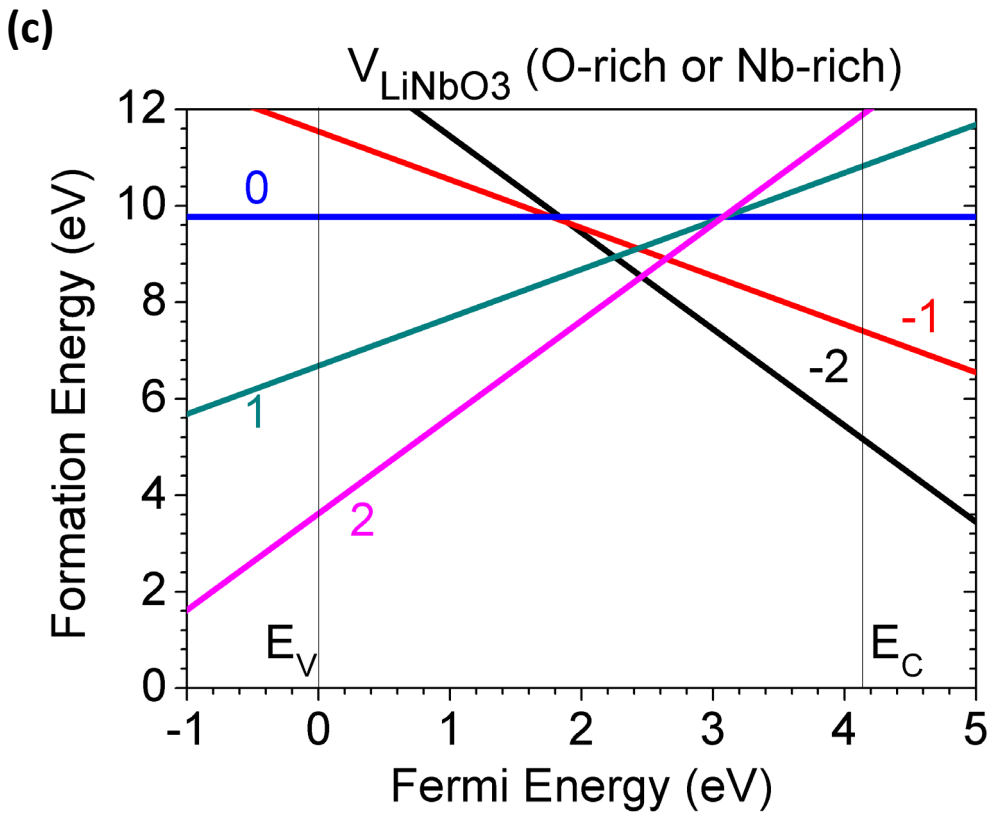

Figure 10. (a) TDOSs of V_{LiNbO3} in charge states of 0, +1, -1, +2, and -2. The dashed line denotes the highest occupied level for electrons. (b) Localized electron and hole orbitals at the relaxed V_{LiNbO3} site (Li=purple, O=red, Nb=cyan). (c) Formation energies of V_{LiNbO3} under O- or Nb- rich chemical potential limits.

Figure 11.

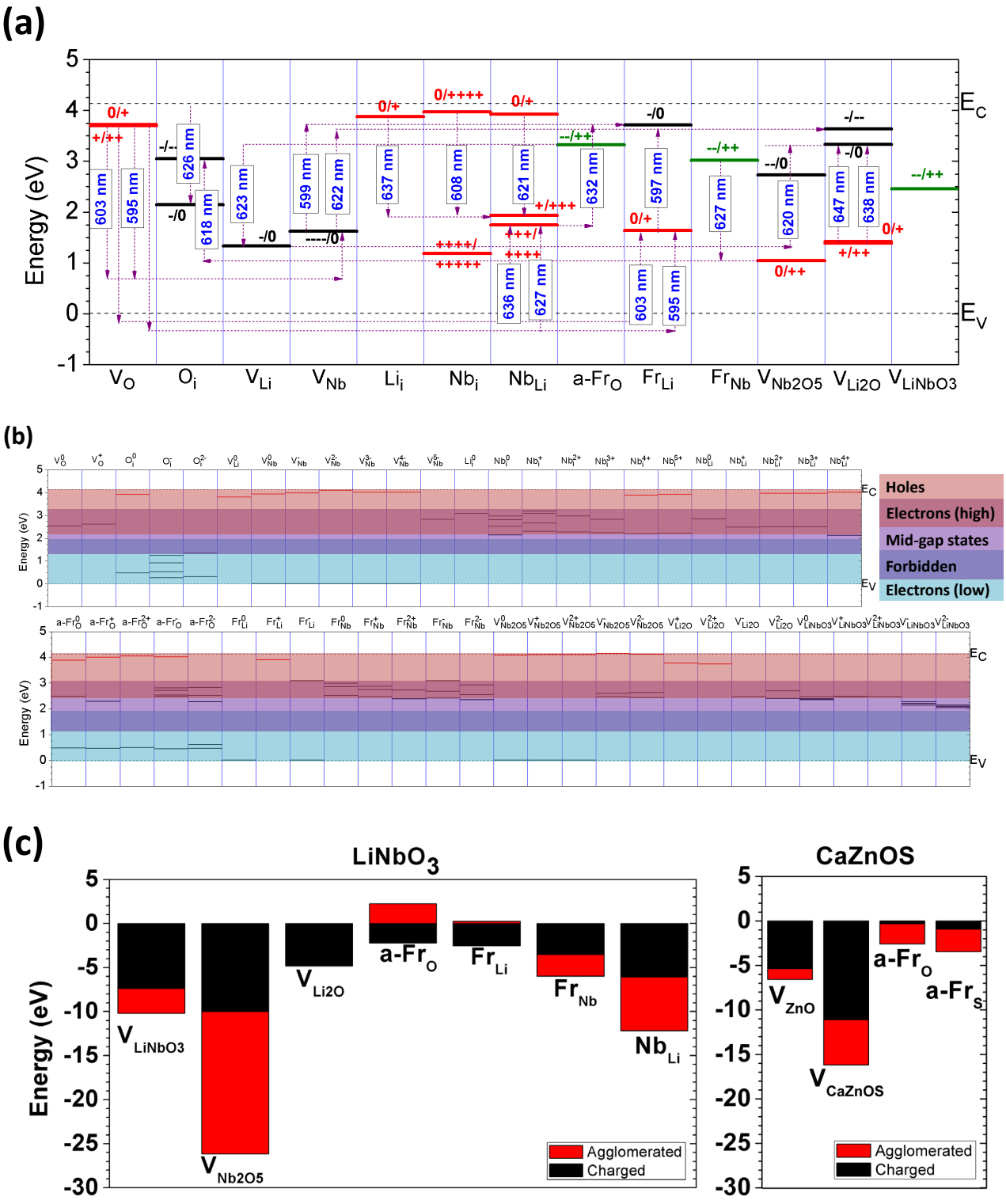
(a)
Energy (eV)
E_C
E_V
V_O
O_i
V_Li
V_Nb
Li_i
Nb_i
Nb_Li
a-Fr_O
Fr_Li
Fr_Nb
V_Nb2O5
V_Li2O
V_LiNbO3
(b)
Holes
Electrons (high)
Mid-gap states
Forbidden
Electrons (low)
(c)
LiNbO3
CaZnOS
V_LiNbO3
V_Nb2O5
V_Li2O
a-Fr_O
Fr_Li
Fr_Nb
Nb_Li
V_ZnO
V_CaZnOS
a-Fr_S
Agglomerated
Charged

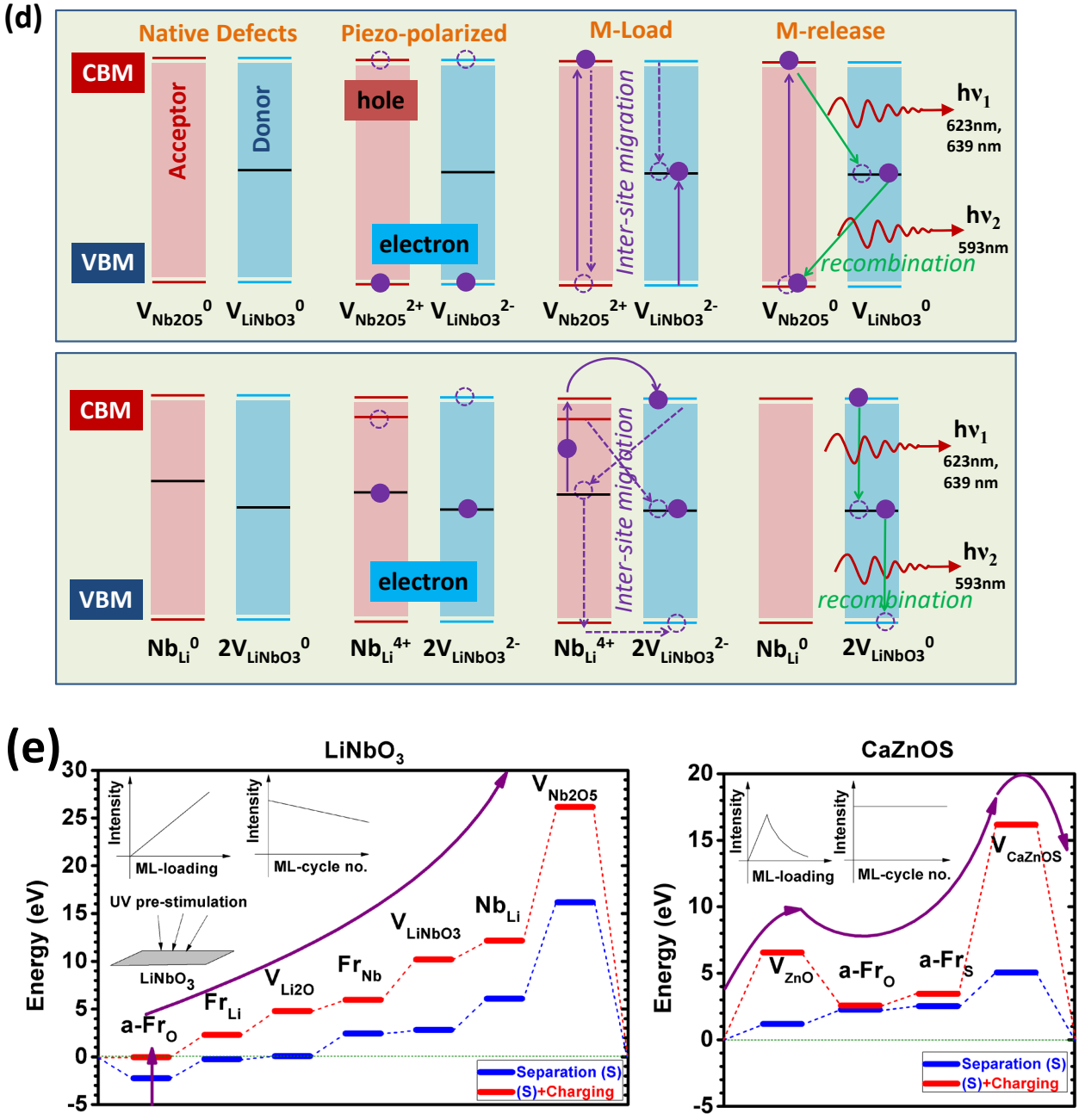

Figure 11. (a) Summary of thermodynamic transition levels of different charge states of the intrinsic defects $LiNbO_3$. The red line denotes donor type transition level and black line shows the acceptor level. (b) Summarized single-particle levels of intrinsic defects in $LiNbO_3$ with different charge states (empty states=red, filled states=black). (c) Summarized energy variation diagram for both $LiNbO_3$ and our previous studied CaZnOS systems to demonstrate the complementarily charged and agglomerated evolutions from point defects to the complex defects responsible for active center for ML energy transfer and electronic transitions. (d) The schematic energy transfer related electronic transitions for the elastic ML photon output. (e) Free energy variation pathway along different native complex defects in both up-doped $LiNbO_3$ and CaZnOS.

References

[1] Z. L. Wang, Nano Today **5**, 540 (2010).
[2] W. Wu and Z. L. Wang, Nature Reviews Materials, 16031 (2016).
[3] X. Wang, et al., Adv. Mater. **27**, 2324 (2015).
[4] D. Peng, B. Chen, and F. Wang, Chempluschem **80**, 1209 (2015).
[5] D. Tu, C.-N. Xu, Y. Fujio, and A. Yoshida, Light Sci Appl **4**, e356 (2015).
[6] H. Zhang, D. Peng, W. Wang, L. Dong, and C. Pan, J. Phys. Chem. C **119**, 28136 (2015).
[7] N. A. Atari, Phys. Lett. A **90**, 93 (1982).
[8] S. Timilsina, K. H. Lee, I. Y. Jang, and J. S. Kim, Acta Mater. **61**, 7197 (2013).
[9] S. M. Jeong, S. Song, and H. Kim, Nano Energy **21**, 154 (2016).
[10] H. Fang, et al., Nanoscale **7**, 17306 (2015).
[11] Y. Zhang, G. Gao, H. L. W. Chan, J. Dai, Y. Wang, and J. Hao, Adv. Mater. **24**, 1729 (2012).
[12] M.-C. Wong, L. Chen, M.-K. Tsang, Y. Zhang, and J. Hao, Adv. Mater. **27**, 4488 (2015).
[13] L.-B. Huang, G. Bai, M.-C. Wong, Z. Yang, W. Xu, and J. Hao, Adv. Mater. **28**, 2744 (2016).
[14] J.-C. Zhang, C.-N. Xu, S. Kamimura, Y. Terasawa, H. Yamada, and X. Wang, Opt. Express **21**, 12976 (2013).
[15] D. Tu, C.-N. Xu, A. Yoshida, M. Fujihala, J. Hirotsu, and X.-G. Zheng, Adv. Mater. **29**, 1606914 (2017).
[16] X. Wang, C. N. Xu, H. Yamada, K. Nishikubo, and X. G. Zheng, Adv. Mater. **17**, 1254 (2005).
[17] H. Fang, X. Wang, Q. Li, D. Peng, Q. Yan, and C. Pan, Advanced Energy Materials **6**, 1600829 (2016).
[18] Z. L. Wang, The Journal of Physical Chemistry Letters **1**, 1388 (2010).
[19] Y. Liu, S. Niu, Q. Yang, B. D. B. Klein, Y. S. Zhou, and Z. L. Wang, Adv. Mater. **26**, 7209 (2014).
[20] A. Jana and R. E. García, Nano Energy **41**, 552 (2017).
[21] J. Zhang, Nano Energy **41**, 460 (2017).
[22] H. Fang, H. Tian, J. Li, Q. Li, J. Dai, T.-L. Ren, G. Dong, and Q. Yan, Nano Energy **20**, 48 (2016).
[23] L. Chen, M.-C. Wong, G. Bai, W. Jie, and J. Hao, Nano Energy **14**, 372 (2015).
[24] S. Singh and N. Khare, Nano Energy **38**, 335 (2017).
[25] S. Singh and N. Khare, Nano Energy **42**, 173 (2017).
[26] X. Yu, S. Wang, X. Zhang, A. Qi, X. Qiao, Z. Liu, M. Wu, L. Li, and Z. L. Wang, Nano Energy **46**, 29 (2018).
[27] Y. Zhang and L. Li, Nano Energy **22**, 533 (2016).
[28] D. Q. Zheng, Z. Zhao, R. Huang, J. Nie, L. Li, and Y. Zhang, Nano Energy **32**, 448 (2017).
[29] C. Wang, R. Bao, K. Zhao, T. Zhang, L. Dong, and C. Pan, Nano Energy **14**, 364 (2015).
[30] G. Hu, W. Guo, R. Yu, X. Yang, R. Zhou, C. Pan, and Z. L. Wang, Nano Energy **23**, 27 (2016).
[31] X. Wen, W. Wu, C. Pan, Y. Hu, Q. Yang, and Z. Lin Wang, Nano Energy **14**, 276 (2015).
[32] J.-C. Zhang, L.-Z. Zhao, Y.-Z. Long, H.-D. Zhang, B. Sun, W.-P. Han, X. Yan, and X. Wang, Chem. Mater. **27**, 7481 (2015).
[33] M. Liu and D. Xue, Solid State Ionics **177**, 275 (2006).

[34] Y. Ding, J. Gu, J. Ke, Y.-W. Zhang, and C.-H. Yan, Angew. Chem. Int. Ed. **50**, 12330 (2011).
[35] S. C. Abrahams and P. Marsh, Acta Crystallographica Section B **42**, 61 (1986).
[36] C. J. Pickard, B. Winkler, R. K. Chen, M. C. Payne, M. H. Lee, J. S. Lin, J. A. White, V. Milman, and D. Vanderbilt, Phys. Rev. Lett. **85**, 5122 (2000).
[37] B. Huang, Solid State Commun. **230**, 49 (2016).
[38] B. Huang, Solid State Commun. **237–238**, 34 (2016).
[39] S. J. Clark, M. D. Segall, C. J. Pickard, P. J. Hasnip, M. I. J. Probert, K. Refson, and M. C. Payne, Zeitschrift Fur Kristallographie **220**, 567 (2005).
[40] L. Kleinman and D. M. Bylander, Phys. Rev. Lett. **48**, 1425 (1982).
[41] S. G. Louie, S. Froyen, and M. L. Cohen, Phys. Rev. B **26**, 1738 (1982).
[42] A. M. Rappe, K. M. Rabe, E. Kaxiras, and J. D. Joannopoulos, Phys. Rev. B **41**, 1227 (1990).
[43] P. J. Hasnip and C. J. Pickard, Comput. Phys. Commun. **174**, 24 (2006).
[44] K. Laasonen, A. Pasquarello, R. Car, C. Lee, and D. Vanderbilt, Phys. Rev. B **47**, 10142 (1993).
[45] N. Marzari, D. Vanderbilt, and M. C. Payne, Phys. Rev. Lett. **79**, 1337 (1997).
[46] M. I. J. Probert and M. C. Payne, Phys. Rev. B **67**, 075204 (2003).
[47] I. A. Vladimir, F. Aryasetiawan, and A. I. Lichtenstein, J. Phys. Condens. Matter **9**, 767 (1997).
[48] S. Lany and A. Zunger, Phys. Rev. B **80**, 085202 (2009).
[49] S. Lany and A. Zunger, Phys. Rev. B **81**, 205209 (2010).
[50] B. J. Morgan and G. W. Watson, J. Phys. Chem. C **114**, 2321 (2010).
[51] P. R. L. Keating, D. O. Scanlon, B. J. Morgan, N. M. Galea, and G. W. Watson, J. Phys. Chem. C **116**, 2443 (2011).
[52] B. Huang, R. Gillen, and J. Robertson, J. Phys. Chem. C **118**, 24248 (2014).
[53] B. Huang, Philosophical Magazine **94**, 3052 (2014).
[54] B. Huang, J. Comput. Chem. **37**, 825 (2016).
[55] T. Zacherle, A. Schriever, R. A. De Souza, and M. Martin, Phys. Rev. B **87**, 134104 (2013).
[56] B. Huang, Phys. Chem. Chem. Phys. **19**, 8008 (2017).
[57] B. Huang, Phys. Chem. Chem. Phys. **18**, 13564 (2016).
[58] B. Huang, Inorg. Chem. **54**, 11423 (2015).
[59] S. Lany and A. Zunger, Phys. Rev. B **78**, 235104 (2008).
[60] D. B. Laks, C. G. Van de Walle, G. F. Neumark, P. E. Blöchl, and S. T. Pantelides, Phys. Rev. B **45**, 10965 (1992).
[61] S.-H. Wei, Comp. Mater. Sci. **30**, 337 (2004).
[62] G. Makov and M. C. Payne, Phys. Rev. B **51**, 4014 (1995).
[63] R. S. Weis and T. K. Gaylord, Applied Physics A **37**, 191 (1985).
[64] H. D. Megaw and C. N. W. Darlington, Acta Crystallogr. A **31**, 161 (1975).
[65] H. Boysen and F. Altorfer, Acta Crystallographica Section B **50**, 405 (1994).
[66] J. Zhu, S. Zhao, D. Xiao, X. Wang, and G. Xu, J. Phys.: Condens. Matter **4**, 2977 (1992).
[67] D. Redfield and W. J. Burke, J. Appl. Phys. **45**, 4566 (1974).
[68] S. Kase and K. Ohi, Ferroelectrics **8**, 419 (1974).
[69] Y. Li, W. G. Schmidt, and S. Sanna, Phys. Rev. B **89**, 094111 (2014).
[70] W. G. Schmidt, M. Albrecht, S. Wippermann, S. Blankenburg, E. Rauls, F. Fuchs, C. Rödl, J. Furthmüller, and A. Hermann, Phys. Rev. B **77**, 035106 (2008).
[71] A. Riefer, S. Sanna, A. Schindlmayr, and W. G. Schmidt, Phys. Rev. B **87**, 195208 (2013).

[72] C. Thierfelder, S. Sanna, A. Schindlmayr, and W. G. Schmidt, physica status solidi (c) **7**, 362 (2010).
[73] A. M. Mamedov, M. A. Osman, and L. C. Hajieva, Applied Physics A **34**, 189 (1984).
[74] E. Wiesendanger and G. Güntherodt, Solid State Commun. **14**, 303 (1974).
[75] A. Riefer, M. Friedrich, S. Sanna, U. Gerstmann, A. Schindlmayr, and W. G. Schmidt, Phys. Rev. B **93**, 075205 (2016).
[76] B. Huang, H. Dong, K.-L. Wong, L.-D. Sun, and C.-H. Yan, J. Phys. Chem. C **120**, 18858 (2016).
[77] H. Xu, D. Lee, J. He, S. B. Sinnott, V. Gopalan, V. Dierolf, and S. R. Phillpot, Phys. Rev. B **78**, 174103 (2008).
[78] M. Sun and B. Huang, Inorg. Chem. **56**, 7975 (2017).
[79] H. Donnerberg, S. M. Tomlinson, C. R. A. Catlow, and O. F. Schirmer, Phys. Rev. B **40**, 11909 (1989).
[80] J. Robertson, Eur. Phys. J-appl. Phys **28**, 265 (2004).
[81] K. Xiong, J. Robertson, M. C. Gibson, and S. J. Clark, Appl. Phys. Lett. **87**, 183505 (2005).
[82] K. Xiong and J. Robertson, Appl. Phys. Lett. **95**, 022903 (2009).
[83] B. Huang, Phys. Chem. Chem. Phys. **18**, 25946 (2016).
[84] B. Huang, D. Peng, and C. Pan, Phys. Chem. Chem. Phys. **19**, 1190 (2017).
[85] D. M. Smyth, Prog. Solid State Ch. **15**, 145 (1984).
[86] J. Han, L. Li, M. Peng, B. Huang, F. Pan, F. Kang, L. Li, J. Wang, and B. Lei, Chem. Mater. **29**, 8412 (2017).
[87] B. Huang and M. Sun, Phys. Chem. Chem. Phys. **19**, 9457 (2017).

TOC

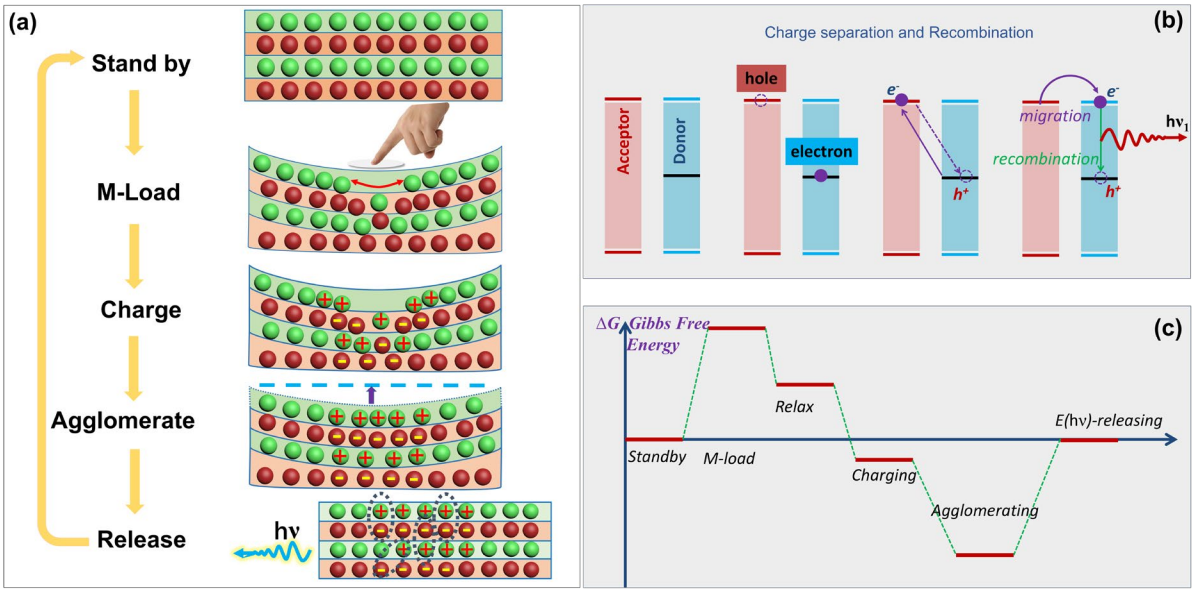

Synopsis (19 words)

Schematic illustrating diagram about the native defects induced energy harvesting and conversion model for the elastic mechano-persistent luminescence (self-recoverable).